Master of Science Thesis

Internal flow of fluidic oscillators

A numerical and experimental investigation

Mirko Sitter

December 8, 2015

Aerodynamics

TU Delft

Faculty of Aerospace Engineering

Delft University of Technology

Internal flow of fluidic oscillators

A numerical and experimental investigation

Master of Science Thesis

For obtaining the degree of Master of Science in Aerospace Engineering
at Delft University of Technology

Mirko Sitter

December 8, 2015

Faculty of Aerospace Engineering · Delft University of Technology

Delft University of Technology

DELFT UNIVERSITY OF TECHNOLOGY
DEPARTMENT OF AERODYNAMICS

The undersigned hereby certify that they have read and recommend to the Faculty of Aerospace Engineering for acceptance the thesis entitled **"Internal flow of fluidic oscillators"** by **Mirko Sitter** in fulfillment of the requirements for the degree of **Master of Science**.

Dated: December 8, 2015

Supervisors:

prof. dr. ir. L.L.M. Veldhuis

dr. M. Kotsonis

dr. D. Ragni

dr. ir. A.H. van Zuijlen

Preface

Creativity; finding new ways and doing things differently. Even in the highly researched field of aerodynamics this still is the main driver for innovation. With countless concepts of reducing aerodynamic drag already introduced thus far, it is a daunting task to look for something new. Something better. When Leo suggested fluidic actuators as a topic for my thesis I had never heard of these devices before, which intrigued me. These self-oscillating fluidic devices have the ability to create a stable oscillating jet without any internal moving parts and can be used to reduce aerodynamic drag with positive overall system efficiency. As only little is known on the internal flow mechanics of these devices, Marios suggested using the novel particle shadow velocimetry technique to visualize the internal flow. There I was, having the chance to work on active flow control devices that were completely new to me with an experimental technique that had yet to be pioneered at our department. This report presents my findings.

As I suspect most people feel when it comes to finishing their thesis work, presenting this work marks the end of an era for me. Starting my life as a student in aerospace engineering the good part of a decade ago I would have never thought it would take me this long. Nevertheless, there is not a lot I would do different in retrospect. It has been a time of learning on many levels and in different fields of expertise, concluded with a strong focus on the field of aerodynamics.

All of this would not have been possible without the unconditional support of Liesbeth Florentie. She is the kindest and most loving person I know, while being a very skilled aerodynamicist as well. She helped me numerous times with mathematics I simply could not solve through the course of my study, took on the tedious task of checking my thesis work after a full day of work and was always there to listen to my frustrations and successes. My mother also took a fair part in the latter, while never pushing me even though she had good reasons to. This work would also not have been possible without the outstanding support of Marios Kotsonis, who really went above and beyond his role as a supervisor to help whenever he could. During the experiments at the low speed laboratory I received a lot support from Leo Molenwijk and Stefan Bernardy. It would not have been possible to fully utilize the amazing facilities there without their help. All of the people in the aerodynamics basement also have a part in this work, being a critical sounding board for many ideas. Marlies Hak definitely had the biggest part in this, also being the one to suggest a numerical study before diving into the experimental analysis.

Hopefully reading this work will inspire you, like investigating the internal working mechanism of fluidic oscillators has inspired me. Indeed they are curious devices, with their potential still largely untapped. They deserve more. And might even become the next big thing in aerodynamic drag reduction with a little more effort from our side.

Table of Contents

List of Figures

List of Tables

Introduction

The ever persisting desire to increase the efficiency of the devices that benefit our modern day lives has not kept clear from the field of aerodynamics. With our current resources of energy becoming ever so scarce, aerodynamic performance has become an important factor for many applications. As a result, aerodynamic drag reduction has become a major field of research over the last decades. Not only aircraft benefit from the increasing body of knowledge. Cars, trucks and wind turbines for example have also become more efficient, not the least due to aerodynamic improvements. One way of realizing a reduction in aerodynamic drag is by delaying flow separation from the surface or preventing it entirely. This can be achieved by re-energizing the boundary layer near the surface.

Well known means to re-energize the boundary layer are the application of vortex generators or surface roughness. These passive actuators do not require energy input and feedback control in order to work, at the cost of being 'always on' control devices. Active flow control devices have the advantage that they can be switched off and therefore do not generate additional drag when not required. Many types of active flow control devices can be identified, with a useful overview given by Cattafesta and Sheplak (2011). Well-known examples are plasma actuators and steady suction and/or blowing. More recently the utilisation of oscillatory blowing was investigated by Seifert et al. (1993). This has sparked new interest in using fluidic oscillators as active flow control devices, sometimes in combination with boundary layer suction such as the suction and oscillatory blowing actuator introduced by Arwatz et al. (2008b).

These fluidic oscillators have shown very promising results in reducing the aerodynamic drag of bluff bodies (see Seifert et al. (2008) and Wilson et al. (2013)) and increasing the lift over drag ratio of wings (Seele et al. (2009)). The properties of the oscillating flow at the exit, such as the oscillating frequency and the amount of time the exit jet spends fully deflected during an oscillation cycle, fully depends on the internal geometry of the fluidic oscillator. The internal working mechanism of fluidic oscillators differs greatly between fluidic oscillator types and has thus far been analysed for individual oscillators using numerical simulation techniques (e.g. Gokoglu et al. (2010b) and Bobusch et al. (2013b)) and experimental flow visualisation on enlarged geometries (e.g. Gärtlein et al. (2014)).

Scope and objectives

Although many experiments on the external flow and application of fluidic oscillators have been performed, visualisation of the internal flow has been limited to enlarged geometries and numerical simulations. The internal flow of small-scale fluidic oscillators is very difficult to visualise experimentally due to the small and complex geometries. Furthermore, a direct comparison between different types of oscillators was still lacking. In order to expand upon the current understanding of fluidic oscillators the problem of visualizing the internal flow needed to be solved and tested on different fluidic oscillator types. Therefore the following research objective was formulated:

> **The objective of this research is to investigate the internal flow mechanics of small-scale fluidic oscillators in order to identify the main internal flow characteristics and present a comparison between different fluidic oscillator types.**

The approach taken to satisfy this objective consisted of a literature review, numerical simulations and experimental flow field measurement, thereby aiming to answer the following questions:

- How can the different fluidic oscillator types be best categorized?
- What geometries of these different types should be experimentally measured and numerically simulated to obtain a meaningful comparison between types?
- What is a suitable measurement technique to perform internal flow measurements on fluidic oscillators?
- What are the internal flow mechanics of the fluidic oscillators during an oscillation cycle?
- How does the oscillation frequency of the different types vary with inlet flow rate?
- Do the measured and numerically simulated flow characteristics agree qualitatively and quantitatively?
- What are the differences in internal flow mechanics, exit flow characteristics and oscillation frequencies between the different fluidic oscillator types?

The remainder of this text is devoted to answering these questions, by which the main objective will be satisfied.

Structure

The discussion starts in **chapter 1** with background information on the fluidic oscillators by presenting the different types, their internal working mechanisms as understood so far and

the investigated applications for active flow control. The different oscillator geometries that have been numerically simulated and experimentally measured will be presented in **chapter 2**, followed by the numerical approach and experimental approach taken. In **chapter 3** the results of the simulations and experiments are presented per fluidic oscillator type. A comparison of the different types is shown in **chapter 4**, including the introduction of an empirical model for the two-dimensional family of fluidic oscillators used for the numerical simulations. The conclusions are presented in **chapter 5**, followed by recommendations for further research in **chapter 6**.

Chapter 1

Theoretical background

The application of fluidic oscillators for active flow control purposes is a relatively recent development, meriting a review of their origins and state of the art. An introduction to different fluidic oscillator types is presented here, including the current understanding of their internal flow mechanics. Experimentally investigated applications of fluidic oscillators are also discussed, clearly showing the potential of these devices. The last section of this chapter introduces the basic concept of particle shadow velocimetry, while a more detailed explanation of how the technique was used for the current investigation will be given in the next chapter.

A fluidic oscillator can be defined as a device that generates a temporally oscillating jet when supplied with fluid under pressure, as described by Gärtlein et al. (2014) for example. All types of fluids can theoretically be used, but for the current investigation the focus will be on fluidic oscillators using air as the working fluid. Nevertheless, some references to measurements performed on oscillators with water as the working fluid will be made. In order to aid the discussion the different fluidic oscillators will be classified in three different types. Classification in types always brings the risk of a narrow minded view on the matter. Therefore the following types are only suggested to aid in the discussion of the various working principles, not to exclude possible combinations or alternative approaches. Designs using other active flow control devices internally, such as piezoelectric actuators, will not be considered here.

1.1 Bi-stable fluidic oscillators

Bi-stable fluidic oscillators make use of the Coanda-effect where flow attaches to either one of the walls in a divergent exit nozzle or an internal chamber. By introducing a control flow using some sort of feedback mechanism the attached flow is released and attaches to the opposite wall. This process reverses periodically due to the feedback mechanism, resulting

in an oscillation of the flow as already noted by Brown (1964). Sometimes a splitter plate is introduced at the exit, aiding the process and essentially creating two pulsing jets at the exit. An example is the oscillator investigated by Wilson et al. (2013). The control flow and feedback mechanism are what defines these bi-stable fluidic oscillators. Two sub-categories will be discussed here: the double feedback loop fluidic oscillator and the single feedback loop fluidic oscillator.

1.1.1 Double feedback loop

Probably one of the oldest designs, the concept of using two feedback loops to control a sweeping jet was already discovered at the Harry Diamond Research Laboratories some time mid 20^{th}century as noted by Wagner (1969). The resulting fluidic oscillator has been widely used since, mostly with liquids as the working fluid. They are still found in various applications such as car wind-shield washers and shower heads. Because of the characteristic flow at the exit it is frequently referred to as a 'sweeping jet actuator'. Although being a proven concept, only recently interest has sparked in using the actuator with air as the working fluid for flow control purposes. Seele et al. (2009) showed promising results implementing an array of double feedback loop oscillators on a V-22 wing for flow control purposes, after which other applications soon followed.

A first attempt at performing a numerical analysis on the internal flow mechanics of a microfluidic bi-stable amplifier using two feedback loops can be contributed to Wagner et al. (2002). The oscillator with a length of approximately 5.8 mm was discretized into 8 123 nodes and simulated using the ANSYS/FLOTRAN 5.7 software package. The Reynolds averaged Navier-Stokes equations were solved using the $k-\epsilon$ turbulence model. The work contains a comparison of required supply pressures to operate the oscillator and frequency responses at different flow rates.

A more thorough numerical analysis was performed for a range of both subsonic velocities by Gokoglu et al. (2010b) and supersonic operating velocities by Gokoglu et al. (2010a). Their dual feedback loop oscillator was discretized using 134 106 elements, with mesh refinements near the walls. After a comparison of turbulence models it was found that the $k-\omega$ SST model is best suited to simulate the internal flow, although a Reynolds stress model was not considered. The numerical results were compared to measurements of the oscillating frequency performed with hot-wire anemometry at the exit. An example of the initiation of the oscillation at a Mach number of 0.3 as presented by Gokoglu et al. (2010b) can be found in figure 1.1.

Koklu and Melton (2012) were the first to present a detailed experimental investigation of the flow behind a double feedback loop fluidic oscillator, comparing the exit nozzle flow field from particle image velocimetry (PIV) experiments with hot-wire anemometry (HWA) measurements. The set-up consisted of a 1024 x 1280 pixel CCD camera equiped with a 105 mm macro lens, a Nd-Yag laser which operated at 15 Hz and 200 mJ output per pulse and 1 μm smoke particles. Consecutive image pairs were separated by a 2 μs delay. Their measurements showed that the jet spends most time attached to either one of the Coanda

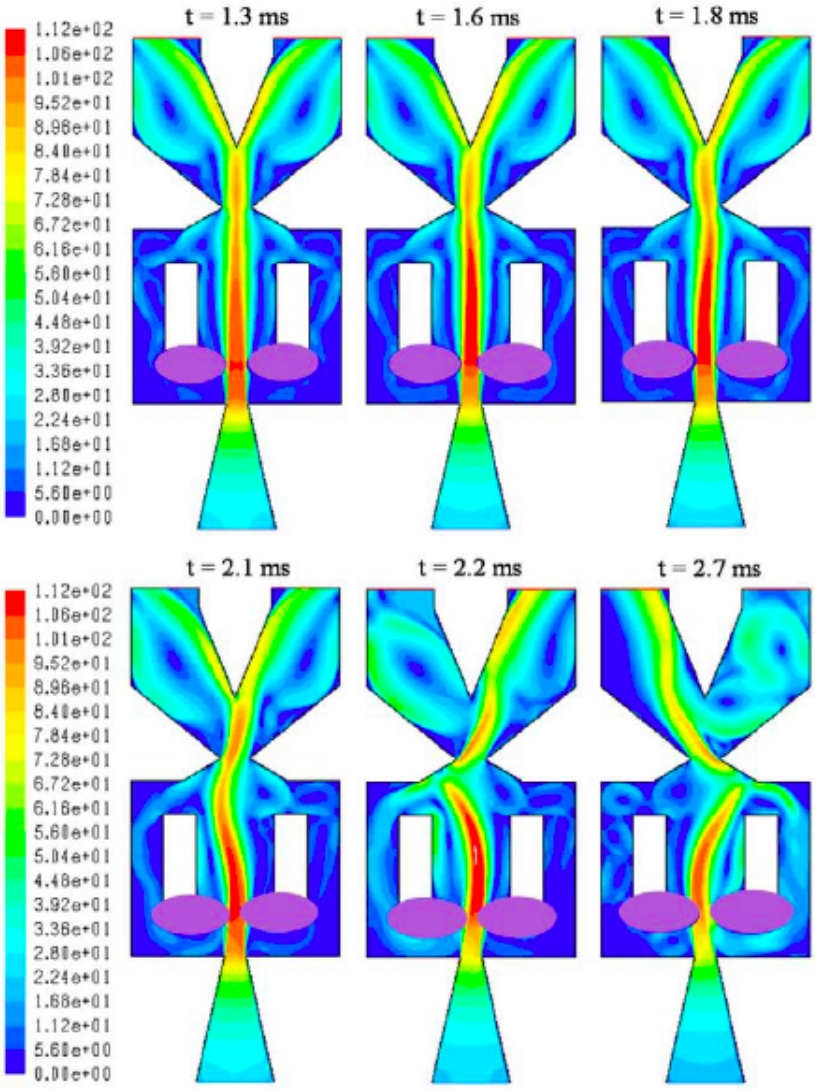

Figure 1.1: Internal velocity magnitude (m/s) contours of a fluidic oscillator obtained by numerical simulation as presented by Gokoglu et al. (2010b), showing the initiation of an oscillation at M=0.3

surfaces and only little time switching from one side to the other. When increasing the mass flow and thus the oscillating frequency, this transition time ratio also increases. Furthermore, the oscillating jet had a spread almost 5 times greater than the non-oscillating equivalent, thus influencing a larger area in flow control applications.

Measurements of the internal flow of a dual feedback loop fluidic oscillator have been performed using water as the working fluid by Bobusch et al. (2013a) and later using air by Gärtlein et al. (2014). The oscillator geometry was cut out of acrylic glass with a refractive index similar to water, being the main motivation of Bobusch et al. (2013a) to use water as the working fluid. Using random PIV snapshots in combination with proper orthogonal decomposition ensured that the obtained phase information was accurate and not biased to-

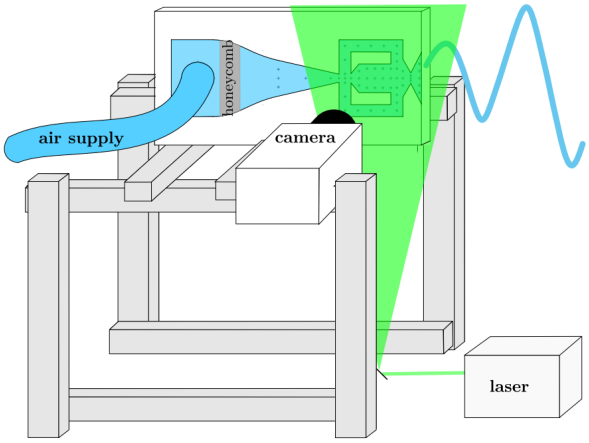

Figure 1.2: Schematic representation of the PIV setup as used by Gärtlein et al. (2014).

wards a dominant oscillation frequency. A similar technique was already used by Koklu and Melton (2012) in their experiments. Ostermann et al. (2014) examined various methods of phase-averaging the oscillating flow in order to increase the accuracy when processing the acquired data. They found that applying an autocorrelation technique helped in identifying the period of a reference signal, which was used by Gärtlein et al. (2014) for their internal flow measurements in air. A schematic representation of their approach is shown in figure 1.2. The PIV measurement data showed the formation of a recirculation bubble after separation from the inlet. The growing bubble pushes the jet in opposite direction, until a new re-circulation bubble is formed on the other side under influence of the feedback tube. This process repeats itself, resulting in an oscillating flow at the exit as illustrated in figure 1.3.

1.1.2 Single feedback loop

Although very similar to the double feedback loop fluidic oscillator, the working principle using a single feedback loop is sufficiently different to justify a separate categorization. It shares the same origin as the double loop variant in the work of Warren at the Harry Diamond Research Laboratories and was first investigated by Viets (1975), but seems to be less represented in literature ever since. That is, until Arwatz et al. (2008b) introduced the suction and oscillatory blowing actuator at the IUTAM Symposium on Flow Control and MEMS in 2008. The suction and oscillatory blowing actuator is a combination of an ejector into a single feedback loop fluidic oscillator. Suction holes feeding into the wake of the ejector increase the mass flow through the oscillator, leading to a very efficient combination of suction and oscillatory blowing when applied to an aerodynamic surface as shown by Seifert et al. (2008), Wilson et al. (2013) and Shtendel and Seifert (2014).

Following the investigations of Arwatz et al. (2008b) a number of internal flow simulations have been performed on the suction and oscillatory blowing actuator. A two dimensional case was investigated by Feikema and Culley (2008), considering only the single feedback loop oscillator using RANS with a k-ω SST turbulence model. It showed a good match

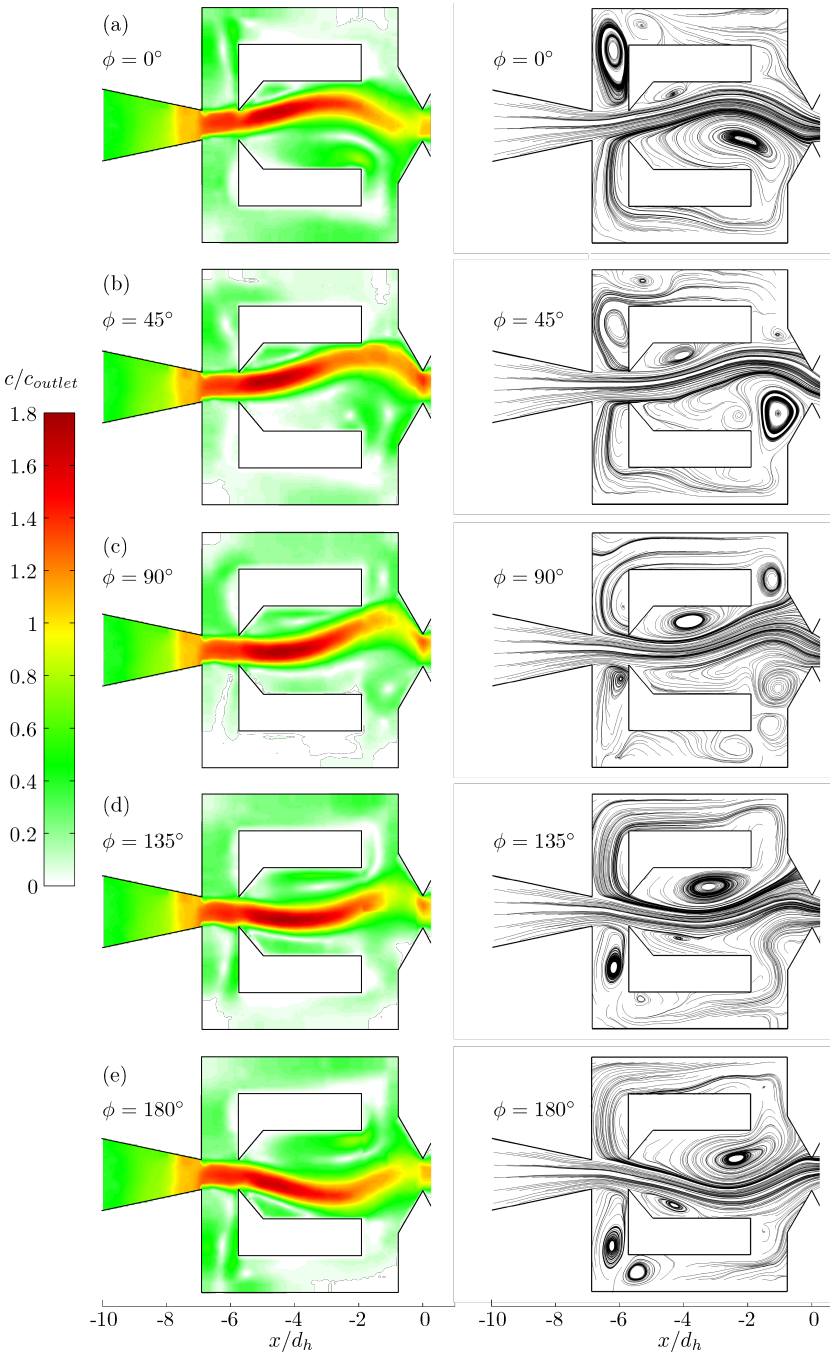

Figure 1.3: Internal flow field and streamlines of a fluidic oscillator as experimentally measured with PIV in air by Gärtlein et al. (2014).

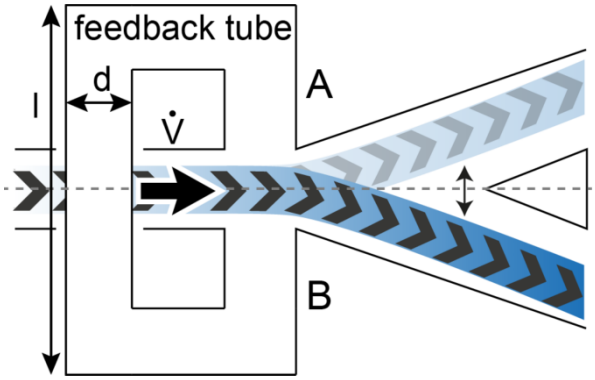

Figure 1.4: Schematic representation of the single feedback loop oscillator of which the internal flow was visualized by Wassermann et al. (2013).

with experimentally measured frequencies. Three-dimensional flow simulations including the ejector for suction have been performed by Kim and Moin (2014). This approach differs from other simulations of fluidic oscillators by including a suction box and plenum to simulate the inlet and outlet flows in addition to the internal flow. Large eddy simulation (LES) solutions are presented using a finite volume discretization of 37 million control volumes. The simulations showed a 27% over-prediction in maximum exit velocity compared to experiments, but measured frequencies match closely.

The internal flow of a single feedback loop oscillator was experimentally visualized using phase-locked three-dimensional three-component (3D3C) magnetic resonance velocimetry (MRV) by Wassermann et al. (2013). The geometry of the oscillator is schematically visualised in figure 1.4. The operating fluid consisted of deionized water with a Gadolinium-based contrast agent and control ports were used to mimic the switching mechanism. They showed that the oscillating flow can be divided into three phases: the stay phase, the detachment phase and the attachment phase.

Using an electrical analogy for the oscillator, Arwatz et al. (2008a) also presented an analytical frequency model. This model allows us to determine the oscillation frequency of a single feedback loop fluidic oscillator by its dimensions and inlet flow conditions as,

$$f = \frac{1}{2\left(\frac{l_t+2l_c}{a} + \frac{0.52}{c}\sqrt{\frac{l_c \cdot d_c}{l_t \cdot d_t}}\frac{Q\rho(l_t+l_c)}{AP_c}\right)}, \tag{1.1}$$

where l_t is the control tube length in m, l_c the control channel length in m, D_t the control tube diameter in m, D_c the control channel diameter in m, Q the flow rate in m^3/s, ρ the air density and a the speed of sound. c and A are empirical constants (2,7 and 0,3 respectively), while P_c is the control pressure, defined as

$$P_c = 32.1Q^2.$$

This model has been validated with experiments and works very well for the actuator dimensions that have been used in the paper of Arwatz et al. (2008b), as shown in figure 1.5.

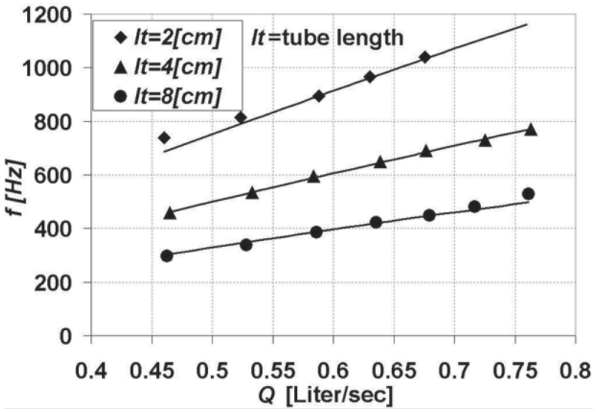

Figure 1.5: Inlet flow rate versus oscillation frequency for the suction and oscillatory blowing actuator investigated by Arwatz et al. (2008b). Both modelling (lines) and experimental results are shown

1.2 Feedback-free fluidic oscillators

Where the previous two types of fluidic oscillators both used the principle of wall attachment due to the Coanda effect as the basis for the switching mechanism, a third type using a different principle can be identified. This type is known as the feedback free fluidic oscillator and basically operates by introducing two jets at a ninety degree angle to each other into a cavity with a single exit near the collision point. The oscillation does not rely on the attachment of the flow to a wall and requires no feedback loop, but results from the interaction of the two jets and internal vortex structures (See Tomac and Gregory (2013)). The design was patented in 2001 by Raghu (2001) and is shown in figure 1.6. The internal flow mechanism was visualised by Tomac and Gregory (2013) using PIV with water as the working fluid in a similar manner as the double feedback oscillator was measured by Bobusch et al. (2013a), clearly showing the different vortex structures that interact to create the oscillatory motion.

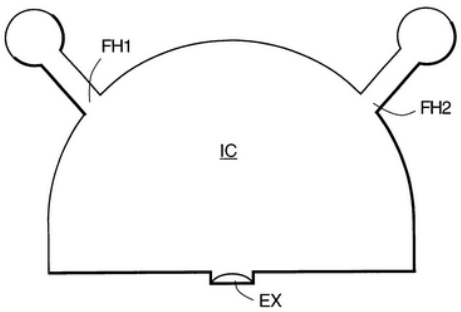

Figure 1.6: Schematic drawing of a feedback-free oscillator with two inlet nozzles as patented by Raghu (2001)

1.3 Application of fluidic oscillators

Active flow control is a highly researched field at the moment; trying to satisfy the demand for improved efficiency in almost every conceivable application. Fluidic actuators are mostly used to delay or prevent boundary layer separation. The idea of delaying separation was already born when Ludwig Prandtl suggested boundary layer suction in 1904, followed by more than a century of research in separation control until now (see Greenblatt and Wygnanski (2000)). While removing the boundary layer before it has the chance to develop and separate has been shown to be effective by Boermans (2006), a more common approach to delay or prevent separation is to add momentum to the boundary layer. Especially close to the wall, where momentum is low, the adverse pressure gradient cannot be overcome. Thus, adding momentum in this region will result in postponed separation. The required momentum can be added by mixing the boundary layer with more energetic flow further from the surface, usually realized by an early transition to turbulence (see Greenblatt and Wygnanski (2000)). Periodic excitation of the boundary layer is a known method to initialize transition and delay the onset of flow separation. A number of actuators producing periodic excitation can be found in literature: the synthetic jet, pulsed jet, moving surface and more recently the plasma actuator. More detailed overviews are given by Gad-el Hak (2013), Cattafesta and Sheplak (2011) and Greenblatt and Wygnanski (2000). The fluidic oscillator has only recently joined the competition, showing promising results so far.

The performance of an array of dual feedback loop fluidic oscillators was first tested in a wind tunnel by Seele et al. (2009) on a V-22 wing. It was suggested that the oscillator was influencing the flow much like a traditional vortex generator would. In the absence of separation the actuation was found to be ineffective, while on the thicker V-22 wing the actuation did influence the flow. This supports the analogy with a vortex generator and Seele et al. (2009) concluded that separated flow is required for the actuator to be useful. With the application on the V-22 wing an increase of the lift over drag ratio of 60% was achieved, as illustrated in Figure 1.7.

A few years later, the effectiveness of using a similar array of dual feedback loop fluidic oscillators to increase the side force on a vertical tail was also investigated by Seele et al. (2012). Three rows of pressure taps were placed on a NACA 0012 airfoil with a 35% flap and 0.538 m MAC, with the actuator array placed at 5% chord of the flap. At a flap deflection of 60% and a free stream velocity of 40 m/s flow separation occurred over the flap. With the actuator array activated complete reattachment of the flow was observed. Furthermore, an increase in side force of at least 50% was measured at varying velocities and actuator momentum input. As vertical tails are dimensioned for incidents such as asymmetric thrust scenarios, being able to increase vertical tailplane effectiveness using these actuators might make smaller dimensions possible. In turn, this could decrease cruise drag significantly.

The flow control properties of the single feedback loop fluidic oscillator in combination with an ejector as developed by Arwatz et al. (2008a) have also been tested on a number of aerodynamic shapes by Seifert et al. (2008), Wilson et al. (2013) and Shtendel and Seifert (2014). Although Sperber already investigated the use of these actuators on a cylinder for his thesis, the first published application was to a bluff body in the shape of a large truck

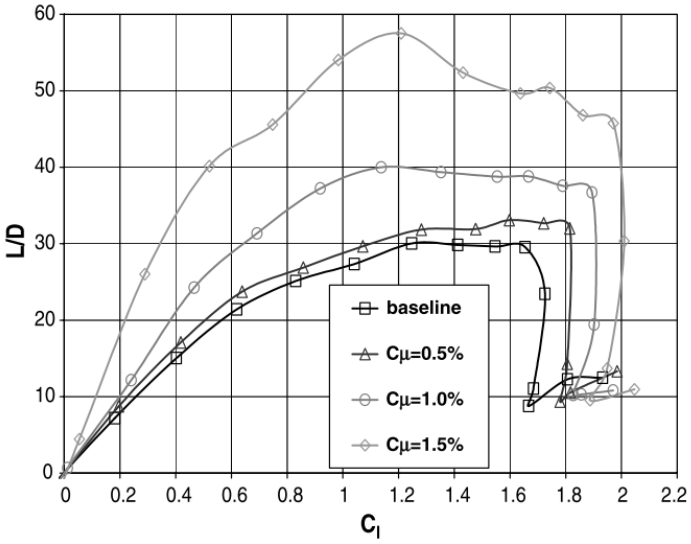

Figure 1.7: V-22 wing L/D at Re 360 000 ($\delta_f = 0$ deg) actuation at 30% flap chord, with C_μ being the actuator supply momentum coefficient, from Seele et al. (2009).

by Seifert et al. (2008). An array of actuators was placed at the upper and lower trailing edge in an attempt to reduce the wake behind the model and thus the aerodynamic drag. The free-stream reference velocity for the experiments was set to 25 m/s, although a range of velocities seem to have been investigated. Considering the optimum between power input to the actuators and their effectiveness an aerodynamic drag reduction of 6-7% was reached with a single array of actuators. Using two arrays, one on either side of the trailer, a drag reduction of 20% was reached. Seifert et al. (2008) claim that this should scale to at least 10% net fuel savings on a full scale truck. Figure 1.8 shows the baseline measured drag, compared to the drag with the individual oscillator arrays activated as well as both of them combined.

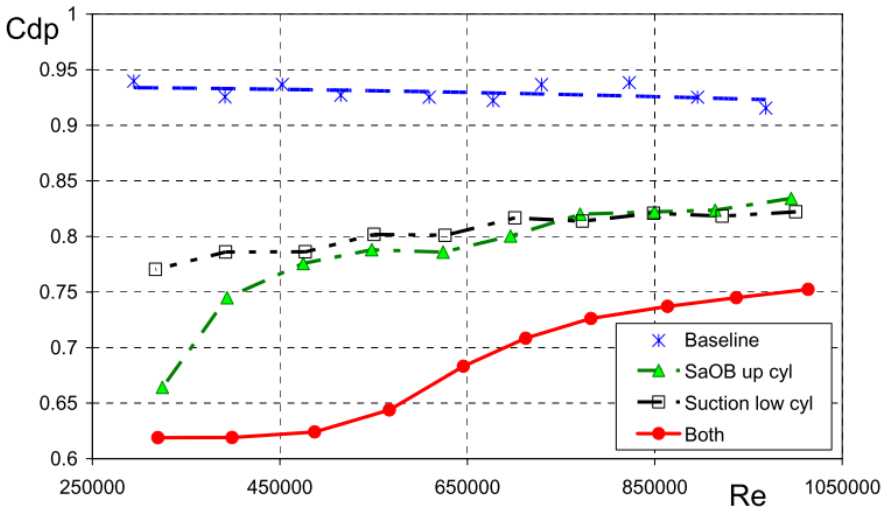

Figure 1.8: Form-drag coefficient of truck model with two oscillator arrays for different Reynolds numbers, by Seifert et al. (2008).

After the combination of suction and oscillatory blowing following the design of Arwatz et al. (2008a) proved to be effective, the application to an axis-symmetric bluff body was investigated by Wilson et al. (2013). The shape was chosen to be similar to a cargo helicopter fuselage. The base experiment was performed for a free-stream velocity of 50 m/s, corresponding to a Reynolds number of $4 \cdot 10^6$. Comparing the results to a numerical analysis and a reference case using only suction on the same body with varying Reynolds numbers resulted in a large parameter space. At low flow control momentum input the drag decrease proved to be most efficient, with an aerodynamic drag reduction around 30% leading to an overall system efficiency increase of 10%. At high momentum input the system showed the ability to delay separation up until the trailing edge.

Although the above gives a good indication of what might be possible using the combination of suction and oscillatory blowing for active flow control in a practical application, perhaps the most exhaustive experimental analysis of the actuator's performance was made by Shtendel and Seifert (2014). Specifically the performance of an actuator array for flow separation delay was investigated, using transitional Reynolds number (50 000 - 250 000) flow over a cylinder. A drag reduction of up to 60% was achieved at full actuation, which did not seem to depend on using 7, 11 or 15 actuators in the array. The best system efficiency was found with low momentum input, being 15% higher than without actuation.

1.4 Particle shadow velocimentry

As the internal flow visualization of fluidic oscillators using PIV seems to be limited to low frequencies and enlarged geometries, a different approach is taken in the current investigation. The required source light for images can be transmitted through the flat sides of the oscillator if they are translucent, therefore particle shadow velocimetry (PSV) is a viable alternative to traditional PIV techniques for this application. Particle shadow velocimetry is a technique that essentially combines backlit particle illumination with traditional PIV techniques, while a narrow depth-of-view is ensured by a high magnification factor and large aperture of the camera lens. A particle shadow velocimetry set-up is schematically represented in figure 1.9. As the light travels in a straight line normal to the focussed plane there should be minimal

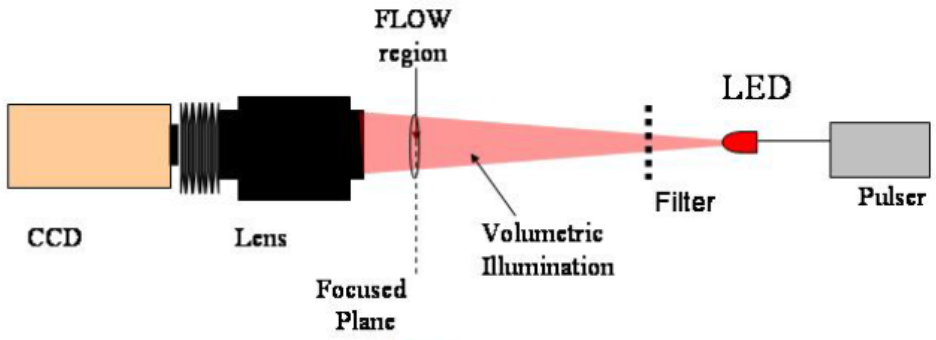

Figure 1.9: Schematic representation of the particle shadow velocimetry set-up used by Estevadeordal and Goss (2005).

refraction given a mismatch in refractive index between air and the translucent material used for the fluidic oscillator side walls, even when curvatures are used in the internal geometry. This eliminates the need to match the refractive index of the working fluid to the acrylic plate material by using water as the working fluid as was done by Bobusch et al. (2013a) and Tomac and Gregory (2013). Gärtlein et al. (2014) did perform PIV measurements on the internal flow of a fluidic oscillator using air as the working fluid, thus having a mismatch in refractive index. The internal geometry of the fluidic oscillator measured did not have any curvatures as shown in figure 1.3, possibly limiting the amount of refracted laser light.

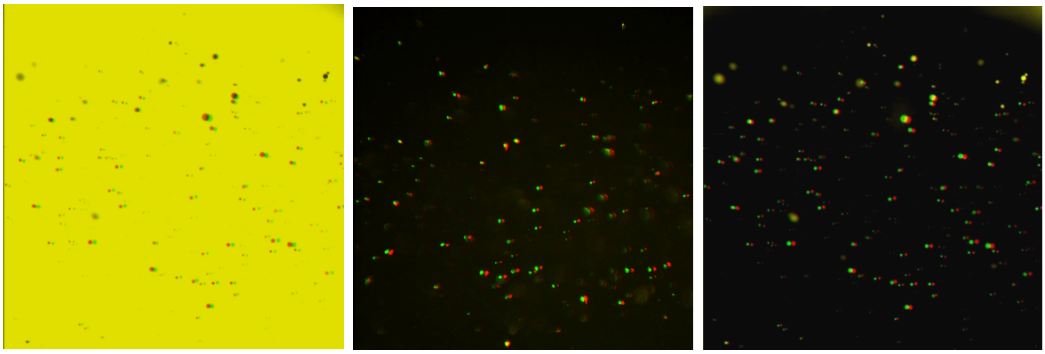

(a) PSV, not inverted (b) PSV, inverted (c) PIV

Figure 1.10: Non-inverted and inverted particle shadow velocimetry image compared to a PIV image using side scattering as shown by Estevadeordal and Goss (2005).

The in-line backlit illumination of the particles results in images that resemble the negatives of images normally used for PIV as shown in figure 1.10 by Estevadeordal and Goss (2005). Using this set-up, Estevadeordal and Goss (2005) showed that PSV is indeed a realistic alternative to traditional PIV. The light source for this kind of experiments would be a high powered LED capable of high frequency light pulses. A number of suitable types were investigated by Willert et al. (2010) specifically for particle image velocimetry applications. Using a custom driving circuit the LEDs can be operated at very high currents with sub-microsecond pulse widths. This arrangement has been shown to work for a number of interesting applications (e.g. Willert et al. (2009), Buchmann et al. (2010) and Geoghegan et al. (2012)). Having a light source capable of high frequency pulses in combination with a high-speed camera ensures the ability to obtain high sampling rates, as would also be possible using traditional PIV. Gärtlein et al. (2014) performed PIV measurements with a sampling rate of 1500 Hz on an enlarged geometry to ensure a temporal resolution that is two orders of magnitude higher than the main oscillation frequency, although there is no evidence to suggest that higher oscillation frequencies can not be measured at similar sampling rates.

Chapter 2

Approach

This chapter will introduce the fluidic oscillator geometries that have been used for the numerical simulations and experiments. Furthermore, the approach to the numerical simulations and particle shadow velocimetry technique to visualize the internal flow of the fluidic oscillators is discussed with the aim to clarify and justify the methodology. The method of reducing the large quantity of data obtained from the simulations and measurements to obtain meaningful results is discussed in the last section of this chapter.

2.1 Fluidic oscillator geometries

The geometries of the three fluidic oscillator types discussed here are chosen such that a comparison of their internal flow characteristics can be made. Their overall dimensions are small, as one would expect for active flow control applications. All oscillators have a total inlet width of 3 mm, resulting in identical flow rates for given inlet velocities. Additionally, all oscillators share the same exit nozzle geometry as shown in figure 2.1. The outer dimensions of the exit were chosen such that they would certainly fit in a single frame during the measurements to have a good reference for the oscillation cycle. The exit nozzle has a 20° divergence angle starting at a 4 mm wide throat with rounded edges, leading towards an 11.28 mm wide exit. During the numerical investigation another exit nozzle that is slightly smaller was also simulated, having a 2 mm wide throat and a 9.28 mm wide exit. The results of the latter variant will not be discussed in detail as they do not match the experimental geometries, but are included in Appendix B. A discussion of the iterative design process that lead to these specific shapes is included in Appendix A. All three geometries presented here are two-dimensional. For the experiments these geometries are cut by laser out of 5 mm thick translucent acrylic plate material, with both sides closed by another 5 mm thick acrylic plate.

The single feedback oscillator (SFO) depicted in figure 2.1 (a) is a rather simple fluidic oscillator geometry, only connecting the walls of the inlet and exit nozzle with a feedback

tube. It has the same operating mechanism as the flip-flop nozzle investigated by Viets (1975). Combining this type with an ejector at the inlet would result in the suction and oscillatory blowing actuator as presented by Arwatz et al. (2008b), although having a shorter exit nozzle with a larger divergence angle and omitting the splitter plate. The feedback length of the SFO was varied between 71.5 mm, 200 mm and 300 mm during the numerical simulations by extending the loop in vertical direction. The 71.5 mm length was chosen as it matches the total length of the two feedback loops of the double feedback oscillator discussed below. During the experiments the feedback length was varied between 150 mm, 200 mm and 300 mm as the tube could not be bend around the oscillator for lengths much smaller than 150 mm.

Figure 2.1 (*b*) shows the geometry of the double feedback oscillator (DFO), having a central mixing chamber with two feedback channels; one on either side of the chamber. The chamber ends in a contraction followed by the diverging exit nozzle. It is essentially a smaller version of the fluidic oscillator geometry investigated numerically by Bobusch et al. (2013b) and experimentally by Bobusch et al. (2013a) and Gärtlein et al. (2014), although having a shorter and thicker mixing chamber in combination with a smaller exit nozzle divergence angle.

The feedback free oscillator (FFO) shown in figure 2.1 (*c*) differs from the two other types in having two inlets and no feedback circuit. The oscillation of the flow at the exit entirely depends on the flow inside the mixing chamber, where two jets at a ninety degree angle to each other collide. Both jets point towards a diverging exit nozzle. The general layout of this feedback free oscillator was patented by Raghu (2001) and later investigated experimentally by Tomac and Gregory (2013). For the experimental measurements, the single inlet nozzle shared by all three oscillators needed to be split into two supply nozzles for the FFO as can be seen in figure 2.4.

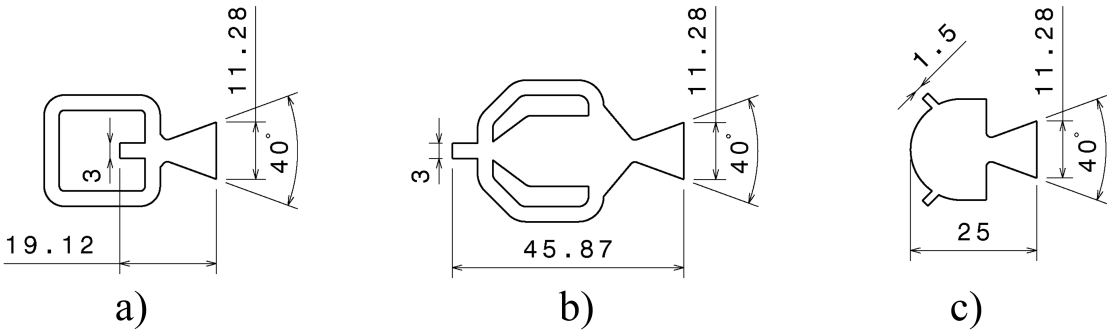

Figure 2.1: Numerically simulated oscillator geometries: a) single feedback oscillator, b) double feedback oscillator and c) feedback free oscillator. Dimensions are in mm.

oscillator type	L [mm]	A [mm^2]	mesh nodes	Δt [s]	simulated flow rates q [m^2/s]
SFO	71.5	318.7	65717	$5 \cdot 10^{-6}$	0.075, 0.150, 0.225, 0.300
SFO	200	704.2	114980	$5 \cdot 10^{-6}$	0.075, 0.150, 0.225, 0.300
SFO	300	1004.2	166858	$5 \cdot 10^{-6}$	0.075, 0.150, 0.225, 0.300
DFO	71.5	633.6	86486	$5 \cdot 10^{-6}$	0.075, 0.150, 0.225, 0.300
FFO	-	343.0	167780	$1 \cdot 10^{-6}$	0.075, 0.150, 0.225, 0.300

Table 2.1: Overview of performed numerical simulations, with L being the feedback tube length, A the total internal surface area and Δt the time step size for the transient simulations

2.2 Numerical approach

In order to analyse the properties of these three different oscillator types, transient numerical simulations have been performed on two-dimensional meshes. The unsteady Reynolds averaged Navier-Stokes equations are solved using the modified Launder-Reece-Rodi Reynolds stress turbulence model as provided in ANSYS Fluent. Implicit time stepping with fixed time step sizes was used to ensure a high temporal resolution of the jet oscillation at the exit. The SFO and DFO have been simulated with a time step size of 5e^{-6} s, while the FFO was simulated using time steps of 1e^{-6} s as it reaches higher oscillation frequencies. The simulations are performed for uniform inlet velocities ranging from 25 m/s to 100 m/s, resulting in flow rates between 0.075 m^2/s and 0.3 m^2/s across the 3 mm wide inlet. A full overview of the numerical simulations that have been performed for both exit dimensions is shown in table 2.1.

Due to the complex internal geometries the SFO and DFO are discretized using unstructured meshes that are symmetrical around the center axis, with structured refinements near the walls. The FFO included additional structured regions within the relatively large mixing chamber, as shown in figure 2.2. Cell face sizes were limited to a maximum of 0.1 mm for all oscillators, resulting in the Courant number ranging from 1.25 to 5 for the chosen fixed time steps and inlet flow rates. A fully resolved sub layer within the boundary was ensured by choosing the near-wall mesh refinements such that the dimensionless wall distance (y$^+$) was always smaller than 1.

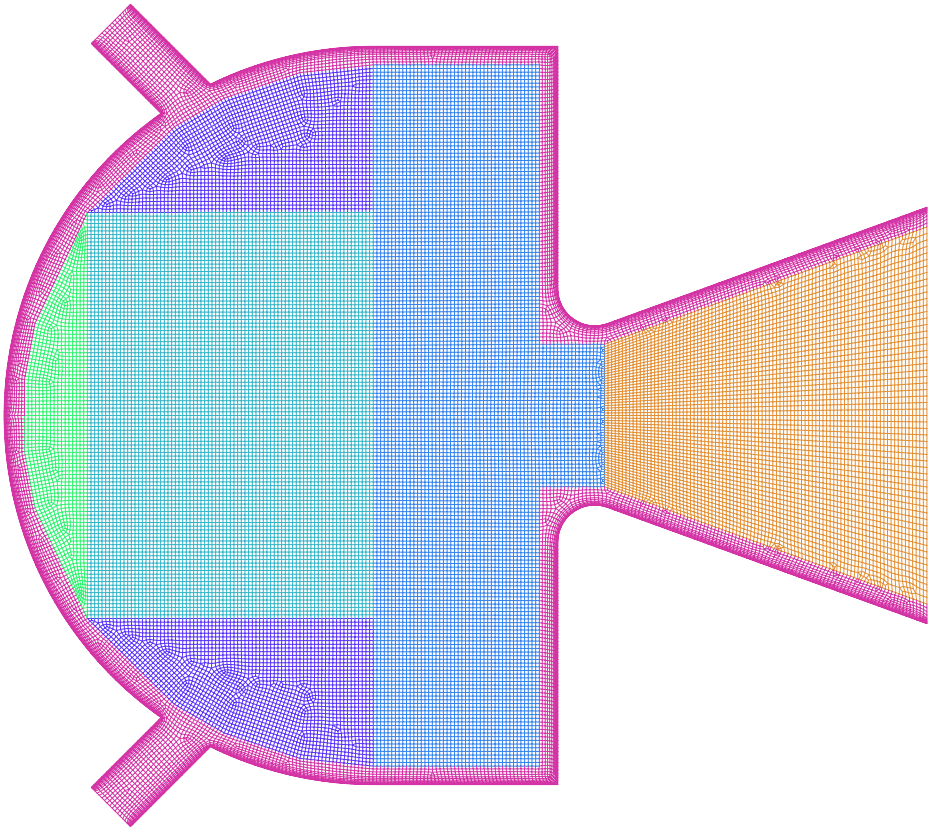

Figure 2.2: Mesh used for the numerical simulations of the feedback free oscillator

2.3 Experimental approach

Due to the curvatures in the internal geometries of the oscillators and the difference in refractive index between perspex material and air it is very difficult to measure the oscillators using traditional PIV techniques. The Particle shadow velocimetry (PSV) technique is suitable to perform experimental internal flow visualisation on fluidic oscillators. With the sides of the oscillators being flat, a light source can shine through the translucent perspex material directly into the camera lens without being refracted, as illustrated in figure 2.3. The shadows of seeding particles travelling with the flow through the oscillators are then captured, producing images that are essentially the inverse of what would be captured using a traditional PIV technique.

Cornstarch particles were used for seeding because oil smoke particles cast shadows that proved to be too small to capture, even at very high magnifications. Estevadeordal and Goss (2005) already used this approach, with good results. However, being a natural product these particles show a large variation in size and density. With particle diameters possibly ranging from 10 μm to 20 μm and their density from 500 kg/m^3 to 700 kg/m^3 it becomes very important to establish their worst-case flow following performance. This can be done

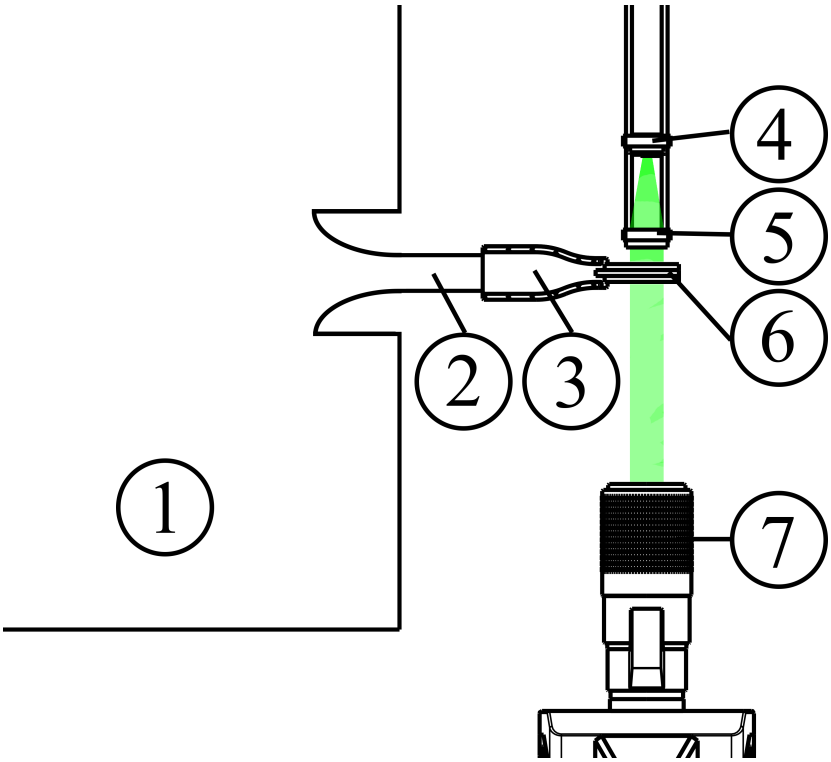

Figure 2.3: Schematic representation of the particle shadow velocimetry set-up with 1) the settling chamber, 2) a circular cross-section contraction, 3) a circular to rectangular cross-section contraction 4) the LED, 5) a lens with semi-translucent sheet, 6) the fluidic oscillator and 7) the high-speed camera. The path of the light is illustrated in green.

using the formulas presented by Mei (1996) to determine the cut-off Stokes number

$$\epsilon_{cutoff} \approx \left[\left(\frac{3}{2\sqrt{\rho}}\right)^{\gamma} + \left(\frac{0.932}{\rho - 1.621}\right)^{\gamma}\right]^{\frac{1}{\gamma}}, \tag{2.1}$$

and the cut-off frequency

$$f_{cutoff} \approx \frac{\nu}{\pi}\left(\frac{\epsilon_{cutoff}}{a}\right)^{2}. \tag{2.2}$$

With a the particle radius, $\nu = 15 \cdot 10^{-6}$ m^2/s the kinematic viscosity of air and $\gamma = 1.05$ this results in a cut-off frequency ranging from 159 Hz to 898 Hz. These are well within the possible operating range of the oscillators, thus limiting the measurements to lower flow rates and corresponding oscillating frequencies. The particles are suspended in the air supply using a cyclone seeder entrained within a pressurized box of 450 L acting as a settling chamber. The air leaves the box through a converging nozzle leading to the 3 mm high and 5 mm deep oscillator inlet.

A green Luminus CBT-120 high-power LED was chosen as the light source, capable of delivering 825 lm when continuously powered with an 18 A supply current. In pulsed operation Willert et al. (2010) showed that even higher currents and corresponding luminous fluxes

can be reached without damaging the LED. A copy of the supply circuit presented in their paper was build and used to operate the LED at the desired sampling frequency. A LaVision Imager pro high speed camera was used to capture the images, featuring a 2016 × 2016 pixel CMOS sensor and a full-frame double exposure sampling rate of 635 fps. Using a 200 mm Nikkor macro objective with extension tubes and reducing the captured frame size resulted in an acquisition rate of 1160 Hz at a field of view of 26 mm × 18 mm. For the feedback free oscillator the frame size was enlarged to obtain a field of view of 30 mm × 22 mm, reducing the acquisition rate to 846 Hz.

The different fields of view required to capture the internal flow of the three fluidic oscillator geometries are shown in figure 2.4. The DFO and FFO require multiple fields of view that need to be stitched. The f-stop of the camera lens was set to a value of 5.6 resulting in a depth of field of approximately 5 mm, with the intention to capture all particle shadows over the full depth of the oscillators. 2000 image pairs were captured during each run, corresponding to measurement times of 1.7 s (SFO and DFO) and 2.4 s (FFO). Three runs were performed for each combination of oscillator geometry, field of view and flow condition. The run showing the highest contrast between seeding particles and background was processed to visualize the internal flow field.

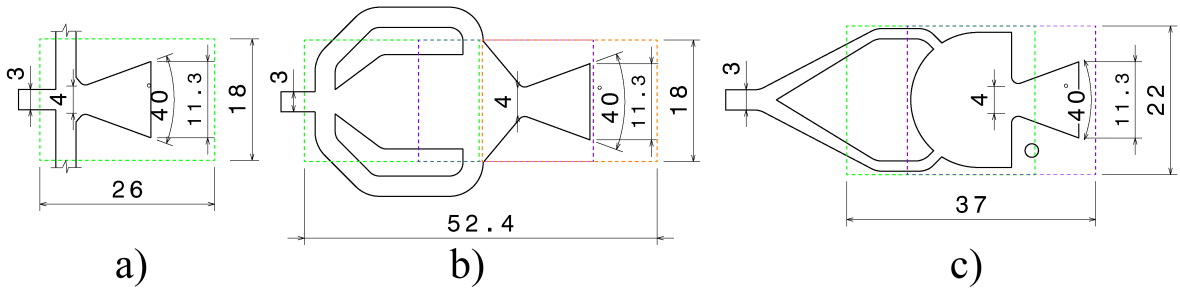

Figure 2.4: Different fields of view for imaging the: a) single feedback oscillator, b) double feedback oscillator, c) feedback free oscillator. Dashed lines show the field of view. Dimensions are shown in mm.

Image pairs with a time delay of 4 μs are analysed using DaVis 8.2 (LaVision GmbH) software. The captured images are the negative of what would be captured using conventional PIV techniques (figure 2.5 *a*) and have to be inverted to facilitate the use of PIV processing algorithms (figure 2.5 *b*), after which the noise floor is reduced by subtracting the minimum of 13 consecutive image pairs (figure 2.5 *c*). Finally, the particle velocities are found by cross-correlating the image pairs in multiple passes with interrogation windows decreasing in size from 128 pixel squares to 32 pixel squares, resulting in the vector fields and velocity contours shown in figure 2.5 (*d*). After processing with the proper orthogonal decomposition technique discussed in the next section, an image as the example shown in figure 2.5 (*e*) can be generated. The final images have a vector density of 8.8 vectors/mm for the SFO and DFO and 8.7 vectors/mm for the FFO.

A test case using a 5 mm high and 5 mm wide channel was used to ensure that the technique described above would provide useful data before measuring the internal flow of fluidic oscillators. Figure 2.6 shows one of the fully processed images at a bulk velocity of 38 m/s.

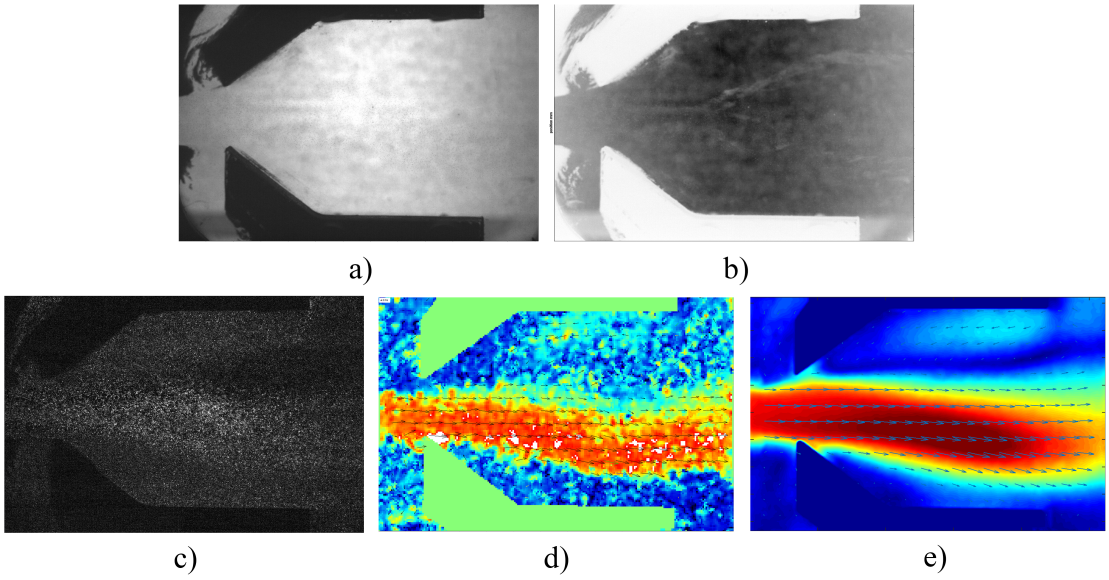

Figure 2.5: Stages of processing the captured image pairs with PSV, with a) the raw image, b) the inverted image, c) the image after subtracting the minimum of 13 consecutive image pairs, d) the resulting velocity contour after correlating a pair and e) the velocity contour after processing with POD.

The PSV technique manages to capture the internal flow surprisingly well, clearly showing a boundary layer within the channel. The velocity profile extracted from the PSV vector field is compared to theoretical models in figure 2.7. The velocity profile does not resemble fully developed laminar pipe flow, but approximately matches the velocity profile modelled with the turbulent power-law velocity equation using n = 10. Due to the short length of the channel the flow is not fully developed.

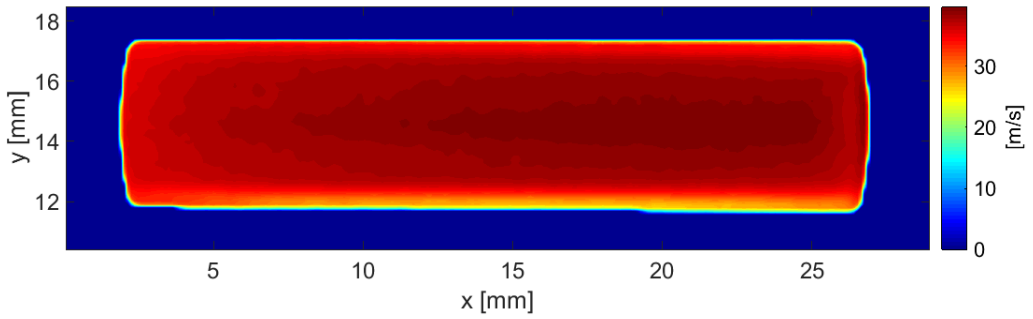

Figure 2.6: Time-averaged flow inside a 5 mm by 5 mm square duct visualised using particle shadow velocimetry with cornstarch particles, showing the potential of the technique

The image shown in figure 2.6 also illustrates some of the potential pitfalls when using the PSV technique, although largely avoidable when the experiments are set-up with care. The main issue was found to be the relatively small size of the LED compared to the measurement area, leading to variations in illumination intensity that are not in-line with the camera. The

errors in the velocity vectors near the left and right edges of the measurement area are a result of this. The problem was largely solved by placing a semi-translucent ('milky') sheet in front of the LED, dispersing the light over a larger area at the cost of reduced luminous intensity. Nevertheless, the outer edges of the measurement area were masked while processing the fluidic oscillator results in order to avoid errors.

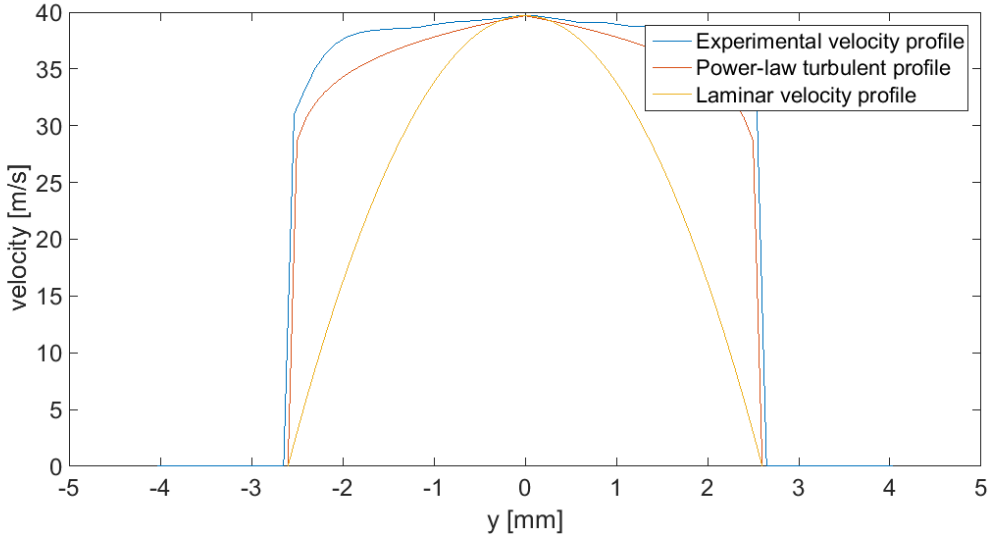

Figure 2.7: Velocity profile inside a 5 mm by 5 mm square duct as measured by PSV and defined by theoretical models for turbulent and laminar flows.

2.4 Data analysis

Both the numerical simulations and experimental measurements resulted in a large amount (approximately 11 TB in total) of data, which needed to be processed to present useful results. This section explains how all the data was processed and how it will be presented for both the numerical and experimental results, as shown in chapter 3.

2.4.1 Numerical simulation

As only the internal flow of the oscillators has been simulated, their oscillating frequencies are determined at the nozzle exit. The position of the exit jet is determined by tracking the peak velocity at the exit at every time step. The most outward deflections are taken as reference points, marking the beginning, half and end of a full oscillation cycle. The oscillation frequency is then determined by the amount of time steps passing between one most outward deflection to the other at the same side. Internal flow visualisations are shown in the form of velocity magnitude contours for half an oscillation cycle, divided into the oscillation phases $\phi = 0$, $\phi = \pi/4$, $\phi = \pi/2$, $\phi = 3\pi/4$ and $\phi = \pi$.

Velocity contours are shown at these oscillation phases to visualize the internal flow mechanics of the oscillators, keeping in mind that the second half of an oscillation cycle would be a mirror image of the first. Additionally, velocities in x-direction are extracted at the exit centre, 4.26 mm above the exit centre and 4.26 mm below the exit centre. The positions are indicated as red dots in figure 2.8, while the green dots are the probe positions for the experimental results. The positions for the experimental measurements have been shifted away from the exit slightly as the end of the acrylic plates casts a shadow, prohibiting the tracking of particles across the exit. The velocities in x-direction at these positions are shown at every time step for a number of oscillation cycles as an indication of the switching speed from one outward deflection to the other and the amount of time the jet stays at either side before switching back. the positions at 4.26 mm above and below the exit center have been chosen as they are close to the diverging walls, but outside the boundary layer.

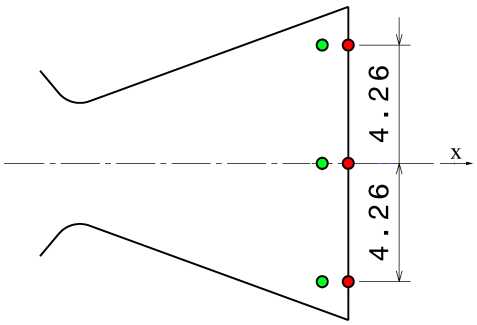

Figure 2.8: Position of shown exit velocities for both the numerical and experimental results. Dimensions are in millimetres.

2.4.2 Particle shadow velocimetry

The calculated velocity vector fields from the particle shadow velocimetry images provide a wealth of information, but also include a lot of noise. Proper orthogonal decomposition (POD) has been used to decompose the velocity data to its main modes over the 2000 image pairs taken per measurement. Only the two most dominant modes have been used to reconstruct the images, aiming to capture most of the physical flow structures while eliminating measurement noise. With the POD modes being based on the eigenvalues of the complete data set, the oscillation frequencies can be extracted by a fast Fourier transform around these eigenvalues. For each oscillator an amplitude spectrum is shown from which the frequency has been extracted. The images of the multiple frames capturing segments of the DFO and FFO were all taken during separate measurements with the same camera and thus needed to be stitched during post-processing. The overlapping area of the images was determined by hand, after which a correlating algorithm matched the best fitting images in the overlapping region. As the measurements were not frequency synchronized with the oscillation the stitched images only represent the closest match to the complete internal vector field.

Two-dimensional inlet flow rates q were extracted from the vector field by calculating the average velocity at the 3 mm high inlet over the entire measurement range. Three dimensional effects such as the boundary layer on the side walls have been neglected in doing so, using

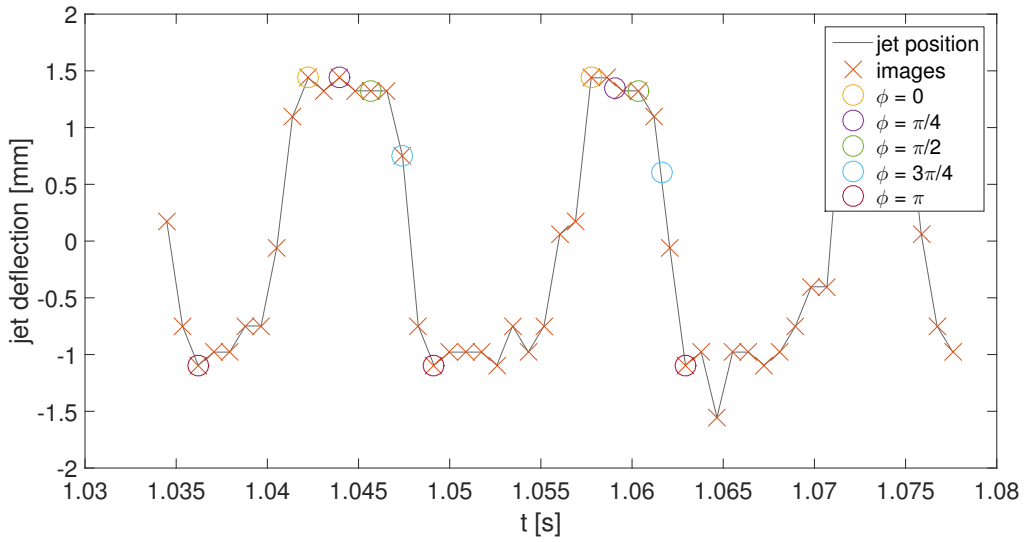

Figure 2.9: Jet position at the exit during a selected range of the SFO measurement at a 0.137 m^2/s inlet flow rate

the assumption that the boundary layer on the side walls is very thin compared to the bulk flow through the centre of the oscillator.

The velocity magnitudes in x-direction at the nozzle exit have been extracted over the entire width of the exit nozzle just before the exit, providing a means to determine the position of the exit jet at every frame. The jet position is defined as the location of the maximum velocity peak in the exit velocity profile. This position can be plotted against time as illustrated in figure 2.9, showing the jet deflection from the centre over a small portion of the entire measurement range for the SFO at a flow rate of 0.137 m^2/s. Knowing that the first occurring most outward deflections during an oscillation cycle are phases $\phi = 0$ (upper) and $\phi = \pi$ (lower), the positions at $\phi = \pi/4$, $\phi = \pi/2$ and $\phi = 3\pi/4$ can also be determined. If at these positions an image pair was taken (indicated by the red crosses in the figure), they can be used to visualize the internal flow at the specified phase of oscillation. For the SFO the first cycle in the range shown in figure 2.9 already contains all required images. For the DFO and FFO the images were selected from a range of different oscillation cycles to obtain the best match, sometimes several hundreds of seconds apart.

As for the numerical results, the velocities in x-direction are shown for a portion of the entire measurement duration at three vertical locations: at the exit centre, 4.26 mm above the exit centre and 4.26 mm below the exit centre. The positions are shown as green dots in figure 2.8. They are not positioned exactly on the exit boundary as was done for the numerical results since the boundary casts a shadow that prohibits the tracking of particles across it. The 4.26 mm positions from the centre are thus closer to the diverging exit nozzle wall than the numerical probes, but still outside the boundary layer. The periodic nature of the velocity magnitude at the exit presents insight in the characteristics of the oscillating jet.

Chapter 3

Results

The results obtained by numerical simulations and experimental measurements for the SFO, DFO and FFO are presented in this chapter. Each section discusses a single oscillator type, divided into the numerical results, experimental results and frequency dependence upon inlet flow rate. A comparison between the three different types based on the results presented here will be made in the next chapter.

3.1 Single feedback oscillator (SFO)

This section presents the results of the numerical and experimental internal flow investigation of the SFO. The numerical results are discussed first, showing internal velocity contours for half an oscillation cycle and probe velocities at the exit for a single inlet flow rate. The experimental results also include velocity contours for half an oscillation cycle and probe velocities at the exit, making a direct comparison possible. Finally, the variation of oscillation frequencies for different inlet flow rates is shown.

3.1.1 Numerical results

The single feedback oscillator with a feedback tube length of 200 mm and an inlet supply rate of 0.150 m^2/s is discussed here, corresponding to an oscillation frequency of 241 Hz. The same oscillator with different feedback tube lengths and inlet flow rates shows similar internal flow characteristics, albeit with smaller deflections for the shortest feedback tube length. When attached to either side of the diverging exit nozzle, the flow is bend inwards and accelerated at the feedback tube opening as shown in figure 3.1 (a). The fluid at this end of the feedback tube is entrained within the jet, creating a very slow flow within the tube pushing the jet in opposite direction. The flow starts separating from the diverging wall

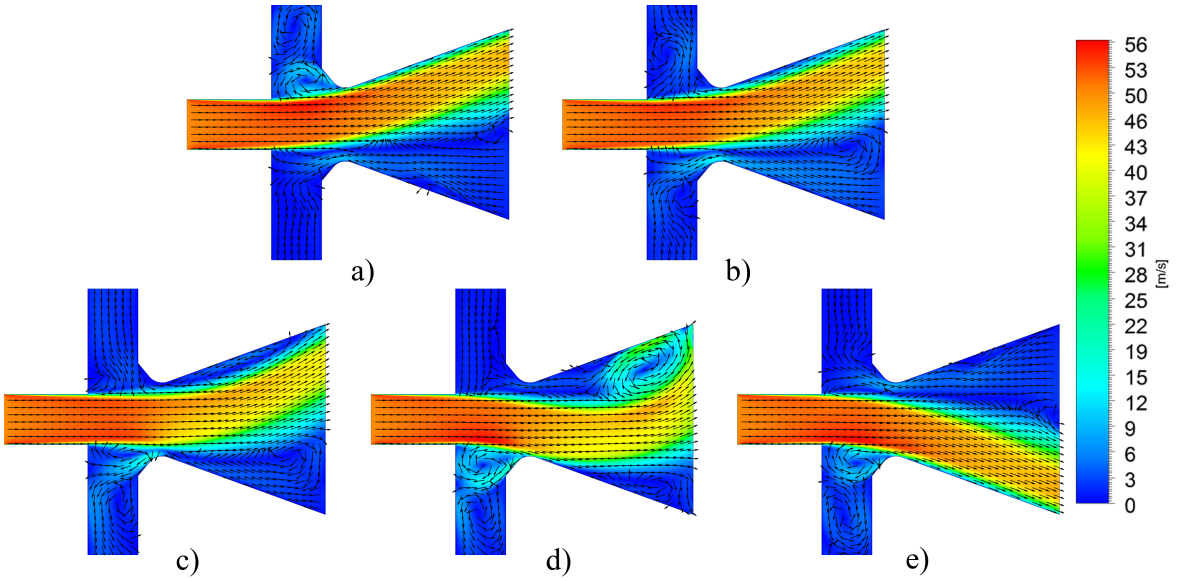

Figure 3.1: Numerically determined velocity contours for the single feedback oscillator at a phase of a) 0, b) $\pi/4$, c) $\pi/2$, d) $3\pi/4$ and e) π

just after the nozzle throat (figure 3.1 *b*), until separation reaches towards the nozzle exit (figure 3.1 *c*). A recirculation is formed within the separated region (figure 3.1 *d*) that moves downstream with the flow. The flow then attaches to the opposite wall near the nozzle throat first, progressing to a fully attached jet as shown in figure 3.1 (*e*).

Figure 3.2 shows the exit velocities in x-direction at three different locations: near the top wall, at the center and near the bottom wall (see figure 2.8). The peak velocity remains at the top or bottom location for a relatively long time, before switching back to the other side very quickly. Using the terminology of Wassermann et al. (2013) the oscillator has a short stay phase followed by a relatively long detachment phase starting with the flow separation near the nozzle throat. This behaviour is also observed in figure 3.1, where three of the five phases in half an oscillation cycle show the jet at one side of the exit. The attachment phase is short as shown by the steep approaches to the maximum velocities at the outer probe positions in figure 3.2. The sudden negative spikes in the graph show the passing of the exit jet followed by a recirculation as captured in figure 3.1 (*d*) . When the jet passes through the center its maximum velocity is just below the maximum velocity while deflected.

3.1.2 Experimental results

As only the first two modes of the POD are used to reconstruct the internal flow fields of the single feedback oscillator it is important to analyse the amount of energy entrained within these two modes compared to the information that is disregarded. Figure 3.21 shows both the relative and cumulative energy entrained within the first 50 modes with a clearly visible peak in the relative amount of energy in the first modes. Almost 24% of the total energy

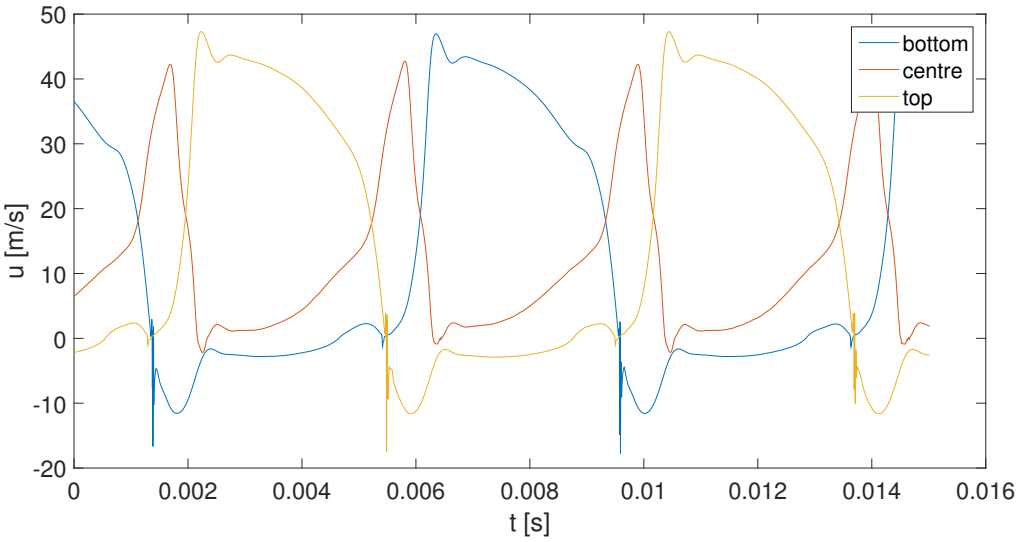

Figure 3.2: Numerically determined velocities in x-direction at the exit centre, 4.26 mm above the exit center and 4.26 mm below the exit center of the SFO

within all 2000 modes is captured by the first two modes, leaving a relatively large amount of noise. Although this could indicate physical flow properties being disregarded as noise, the raw RMS velocity field of figure 3.4 (b) actually shows spots of noise with a relatively high intensity that are not present in the RMS velocity field of figure 3.4 (c) from the reconstructed images.

The mean velocity field of figure 3.4 (a) shows a strong jet through the exit centre, indicating a weak oscillation with only small deviations of the jet from the centre during an oscillation cycle. Additional evidence of this is provided by the RMS velocity contour shown in figure 3.4 (c), having two jet peaks very close to the centre resembling one wide jet.

Being the smallest of the measured fluidic oscillators, the SFO could be captured in a single field of view. It also has the smallest internal resistance, resulting in a higher flow rate at identical inlet pressure compared to the other oscillators discussed here. The mean two-dimensional inlet flow rate of the measurement shown in figure 3.6 was 0.137 m^2/s, neglecting the velocity variations present in the third dimension as the depth of field is small. In combination with a 200 mm long feedback tube this resulted in an oscillating frequency of 70 Hz as shown in the frequency amplitude spectrum of figure 3.5. Although figure 3.6 clearly shows the self-sustained oscillating jet moving from the top a) towards the bottom e), the flow only seems to attach to a small portion of the diverging exit nozzle just after the throat. Attachment of the jet to these surfaces by the Coanda-effect is understood to be an essential part of the switching mechanism as shown in the experiments by Wassermann et al. (2013). The steep diverging angle of 20° is to blame for the rapid separation from the Coanda surface, although still resulting in a stable oscillation.

The consequence of flow separation from the exit nozzle before leaving the oscillator is clearly

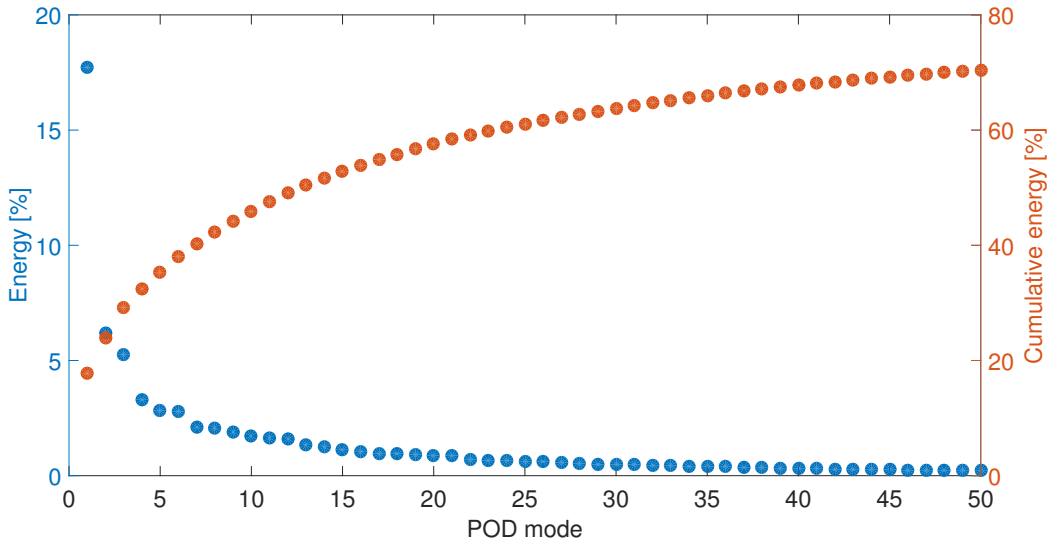

Figure 3.3: Relative and cumulative energy of the first 50 POD modes for the SFO at an inlet flow rate of 0.137 m^2/s

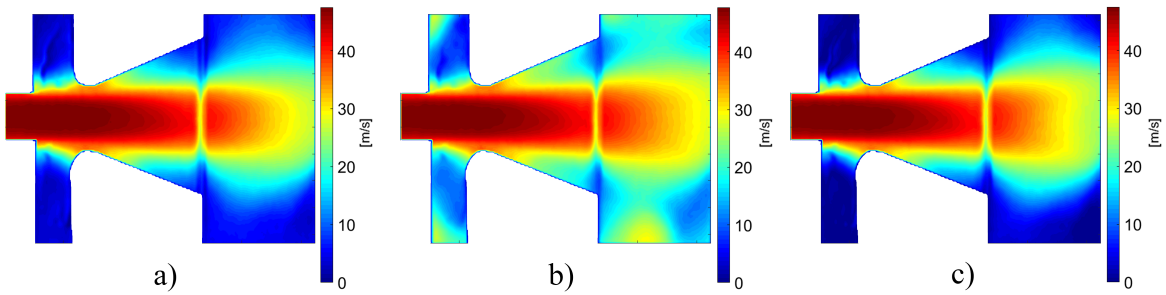

Figure 3.4: Experimental results at the exit for the SFO at an inlet flow rate of 0.137 m^2/s with a) mean velocity contour from POD, b) RMS velocity contour from PSV vector fields and c) RMS velocity contour from POD

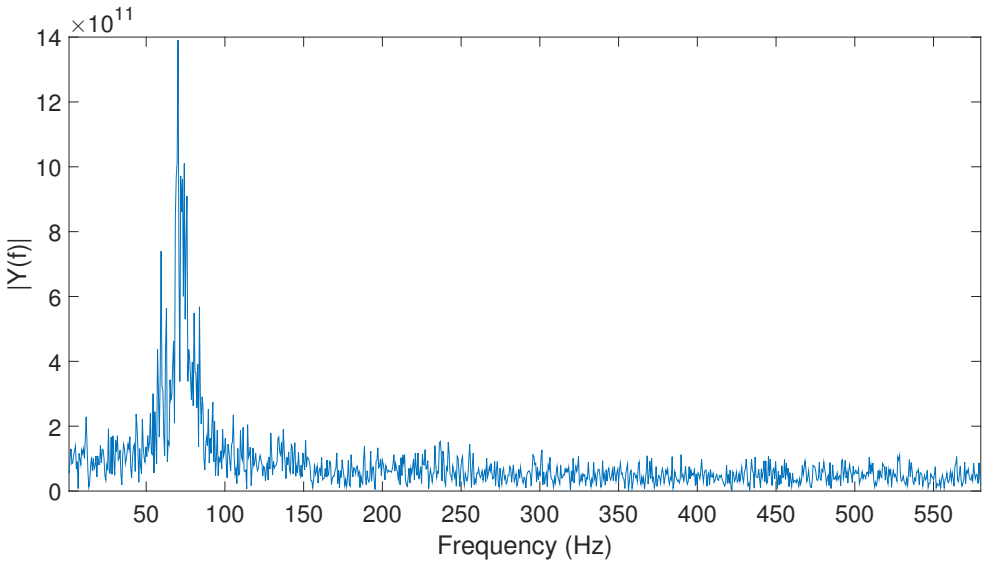

Figure 3.5: Frequency amplitude spectrum for the SFO at an inlet flow rate of 0.137 m^2/s and oscillation frequency of 70 Hz.

shown in figure 3.7, where the velocity at the exit centre is considerably higher than it is closer to the upper and lower wall. The velocities at the top and bottom of the exit do vary in strength at opposite phases as one would expect, becoming slightly negative when the other reaches its maximum. This indicates a recirculation near a wall if the jet is pointing in the opposite direction. Another observation that can be made from figure 3.7 is that the jet remains at one side for some time before switching back to the other, as opposed to reaching an extreme deflection and switching back immediately. This agrees with the numerical simulation results shown in figure 3.2, even though the jet was fully attached to the walls in that case. Contrary to the numerical simulations there seems to be a relatively long stay phase for the measured SFO, with the detachment phase and attachment phase taking an approximately equal amount of time. This is shown by the velocity magnitude plots in x-direction as the decrease in velocity magnitude at an outward position starts with a slow decline in figure 3.2, while the velocity magnitude at an outward position shows a sudden and fast decline in figure 3.7.

3.1.3 Oscillation frequencies

Although the internal flow characteristics are only shown for a single flow rate and feedback tube length, both the numerical simulations and experiments were performed for a range of these variables. Figure 3.8 clearly shows a linear dependence of the oscillation frequency on the inlet flow rate within the measured range. As one would expect the linear lines would extend to a frequency of 0 Hz when there is no flow through the inlet. Although the trend is similar, the deviation of the measured frequencies from the numerical simulations is quite large with an average deviation of 28%. As the inlet flow rates of the measurements were

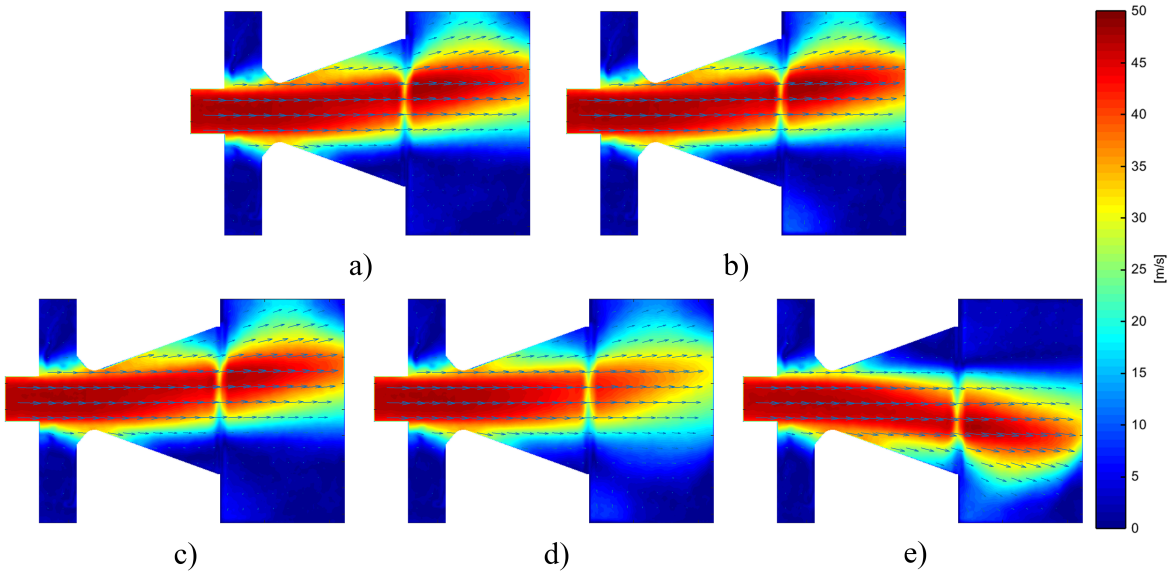

Figure 3.6: Experimentally determined velocity contours for the single feedback oscillator at a phase of a) 0, b) $\pi/4$, c) $\pi/2$, d) $3\pi/4$ and e) π

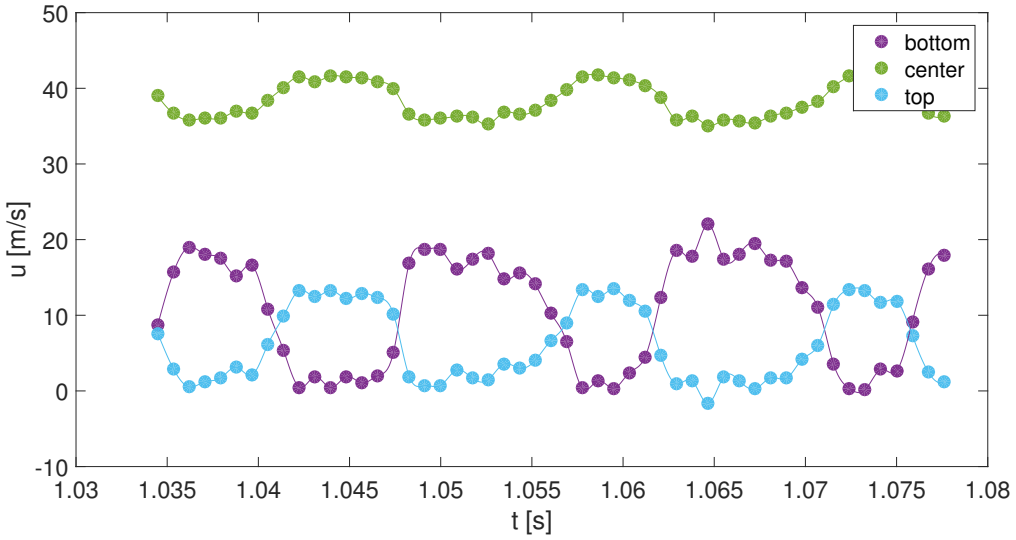

Figure 3.7: Experimentally determined velocities in x-direction at the exit centre, 4.26 mm above the exit center and 4.26 mm below the exit center of the SFO.

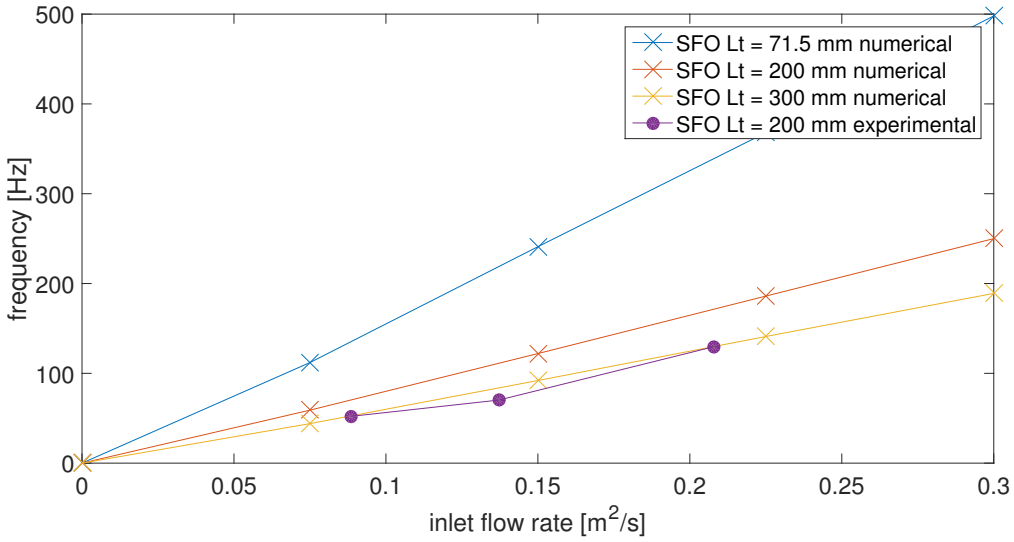

Figure 3.8: Frequency dependence upon inlet flow rate for the single feedback oscillator

only determined from the PSV velocity vectors the errors in this quantity are expected to be large. Furthermore, the velocity at the inlet fluctuated slightly during the measurement, while for the numerical simulations constant inlet velocities were assumed.

The frequency dependence upon the length of the feedback tube is shown in figure 3.9. As the separate experimental measurements had slightly different inlet flow rates fluctuating around 0.13 m^2/s they are shown as individual points. Too little variations were tested to be conclusive, but there seems to be an exponential decay in oscillating frequency with increasing feedback tube length.

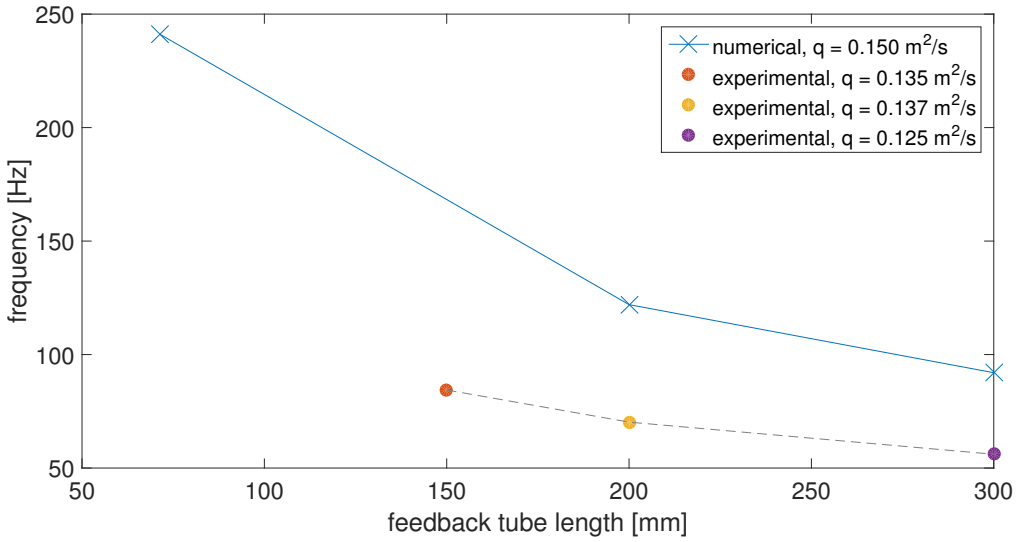

Figure 3.9: Frequency dependence upon feedback tube length for the single feedback oscillator with q being the inlet flow rate

3.2 Double feedback oscillator (DFO)

The results obtained for the DFO by numerical simulation and PSV experiments are discussed in this section. For both the simulations and experiments internal velocity contours are shown for a single inlet flow rate, accompanied by probe velocities at the exit. The frequency dependence upon inlet flow rate is discussed in the last part of this section, presenting a means to quantitatively compare the numerical and experimental results.

3.2.1 Numerical results

The double feedback oscillator shown in figure 3.10 was simulated at the same inlet flow rate of 0.150 m^2/s as the SFO discussed previously, although resulting in a lower oscillation frequency of 110 Hz. The simulations at the other flow rates resulted in similar internal flow fields. One of the first things that can be noticed from the figure is the increased velocity of the jet inside the mixing chamber, reaching up to 66 m/s compared to the 50 m/s at the inlet. While the jet at the exit has reached its top position in figure 3.10 (a), the jet in the mixing chamber is still pointing downward. It continues to move aft and upwards during the first four phases shown, with the jet at the exit slowly moving towards the lower position accordingly. When the jet in the mixing chamber reaches the slant wall leading up to the exit nozzle throat it is deflected downwards, moving the exit jet to its lower extreme outward position in 3.10 (e). The jet inside the mixing chamber moves from one side to the other by the influence of two main circulation regions, which are allowed to grow and move aft by the flow flowing through the feedback loops. This mechanism was already visualized for a similar

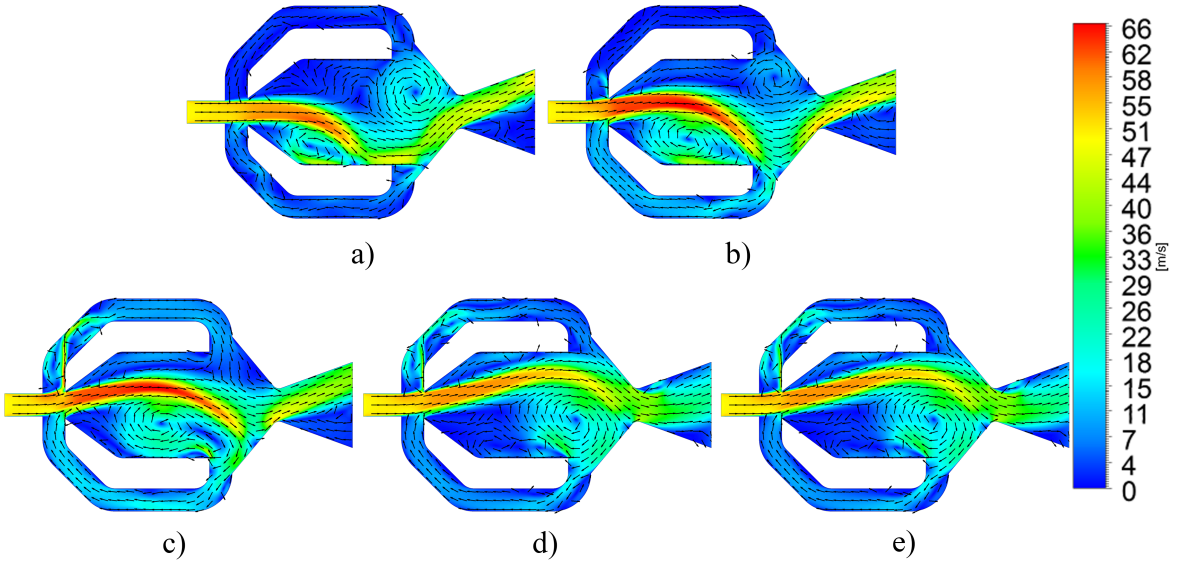

Figure 3.10: Numerically determined velocity contours for the double feedback oscillator at a phase of a) 0, b) $\pi/4$, c) $\pi/2$, d) $3\pi/4$ and e) π

geometry by means of numerical simulations by Bobusch et al. (2013b) and PIV experiments in water by Bobusch et al. (2013a), showing very similar flow structures to what is presented here.

The velocities in x-direction at the exit show large fluctuations while the jet is attached to either wall of the exit nozzle, although steadily switching from one side to the other (figure 3.11). The velocity of the jet is significantly lower when passing the exit centre, while negative velocities near the walls opposite of the attached jet indicate recirculation regions. Compared to the SFO, the DFO has a shorter relative switching time, spending more time of an oscillation cycle fully attached to one side of the exit nozzle. Therefore the DFO can be said to have a long stay phase with a short detachment phase and a very short attachment phase. The quick attachment is enforced by the internal jet being deflected by the slant surface leading up to the exit nozzle.

3.2.2 Experimental results

The first two modes of the proper orthogonal decomposition for the DFO at an inlet flow rate of 0.071 m^2/s entrain almost 31% of the total energy of all 2000 modes, giving a good basis for the reconstruction of the flow field. The relative energy shown in figure 3.12 has a strong peak for the first modes, declining rapidly to less than 1% for the remaining modes. Only the first 50 modes are shown for clarity, with the relative energy of the remaining 1950 modes all approaching zero. The information entrained in these remaining modes accounts for the difference between the RMS flow field of the raw images (figure 3.13 *b*) and the RMS flow field of the reconstructed images (figure 3.13 *c*).

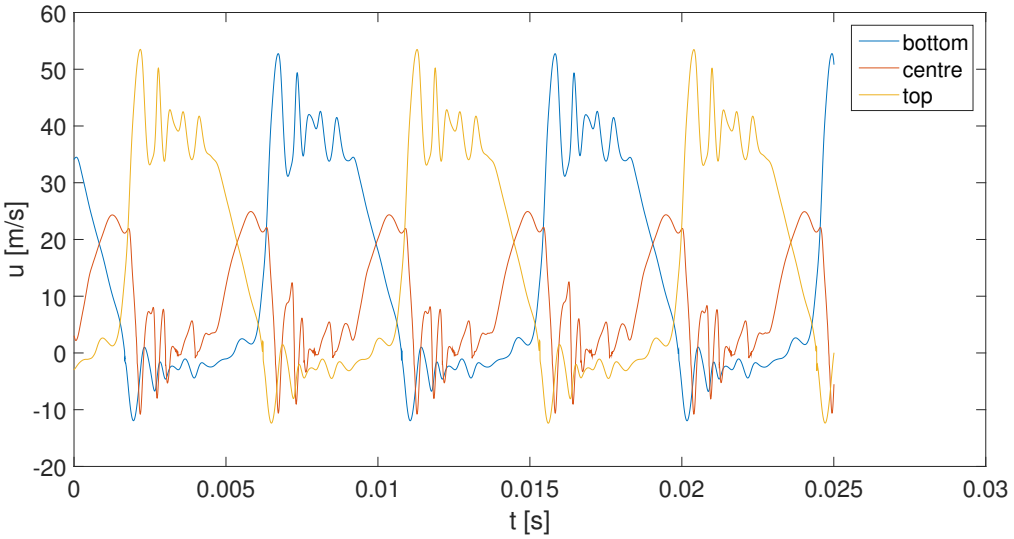

Figure 3.11: Numerically determined velocities in x-direction at the exit centre, 4.26 mm above the exit center and 4.26 mm below the exit center of the DFO

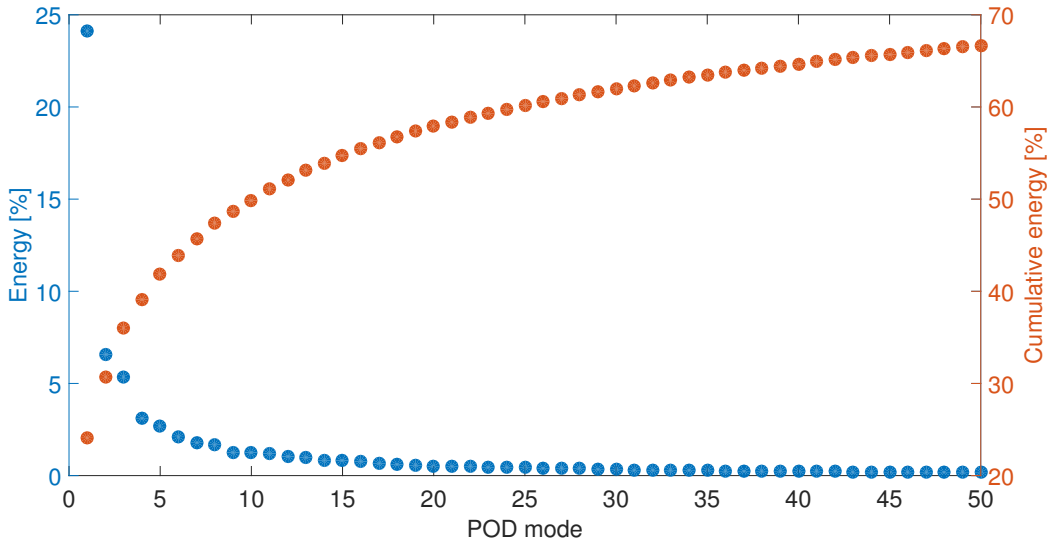

Figure 3.12: Relative and cumulative energy of the first 50 POD modes for the DFO at an inlet flow rate of 0.071 m^2/s

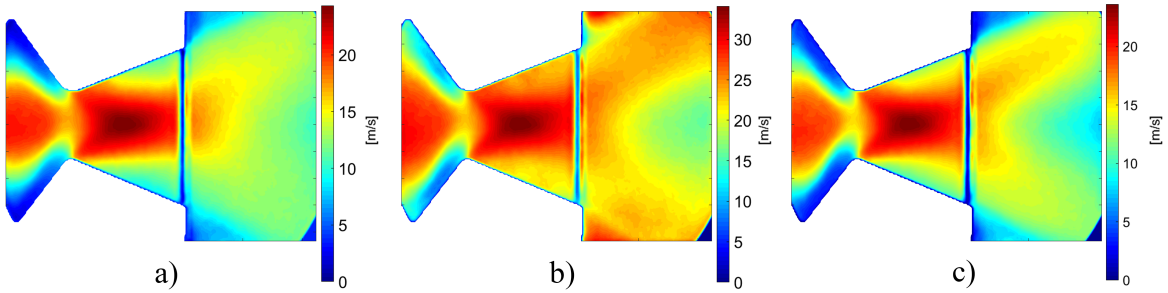

Figure 3.13: Close-up of the experimental results at the exit for the DFO with a) mean velocity contour from POD, b) RMS velocity contour from PSV vector fields and c) RMS velocity contour from POD

The DFO did show a strong oscillation during this measurement with the jet fully attaching to the diverging exit walls during the oscillation cycle, as is apparent from the non-zero mean velocity near the diverging exit walls in figure 3.13 (a). The mean velocity contour of figure 3.13 (a) also shows a large area of influence behind the oscillator exit, which can be favourable for flow control applications. The RMS velocity contour in figure 3.13 (c) shows the strong jet deflection for the DFO, with a weaker influence straight from the exit centre. An asymmetry in the intensity of the upper and lower deflection is also apparent, lacking a physical explanation. The sharp line at the exit with no velocity information in all figures of 3.13 is caused by the shadow of the acrylic plate edge.

The internal flow of the double feedback oscillator was captured at three different fields of view in separate measurements. These were later stitched together by correlating the overlap between images at corresponding phases. A selected set of the resulting snapshots is shown in figure 3.15, again representing half an oscillation cycle. These were taken with a two-dimensional inlet flow rate of 0.071 m^2/s, corresponding to an oscillation frequency of 87 Hz as shown in the frequency amplitude spectrum of figure 3.14. There is a second smaller peak in the frequency amplitude spectrum as well, corresponding to roughly three times the main oscillation frequency. The internal flow of the feedback tubes was not captured, as the walls of the tubes quickly contaminated with seeding material during the measurements. While the jet at the exit is at its upper extreme position in figure 3.15 a), the jet inside the mixing chamber continues to travel upward and aft up until a phase of $3\pi/4$ shown in figure 3.15 d). Here the internal jet hits the slant surface leading up to the exit contraction and is deflected towards the lower extreme position at the exit. Although not as clearly shown as in the numerical simulation results, the internal jet is pushed from one side to the other by the recirculation that is being swept downstream inside the mixing chamber. This corresponds to the findings on a larger scale DFO by Gärtlein et al. (2014). In its outer extreme deflections the exit jet follows the angle of the exit nozzle, thus greater deflections might be possible by increasing the exit nozzle divergence angle. A less obvious difference with the numerical simulations is the widening of the jet inside the mixing chamber in figure 3.15, while the numerical simulation results in figure 3.10 showed the jet from the inlet becoming narrower inside the mixing chamber. This can be explained by the experimental oscillator being supplied with air under pressure, while the numerical simulations had constant inlet velocity boundary conditions.

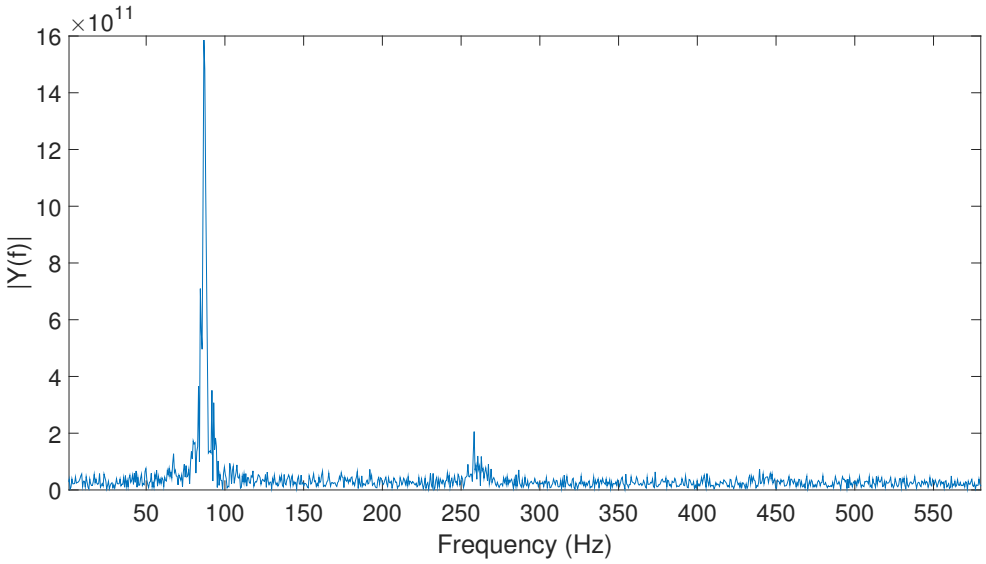

Figure 3.14: Frequency amplitude spectrum for the DFO at an inlet flow rate of 0.071 m^2/s and oscillation frequency of 87 Hz

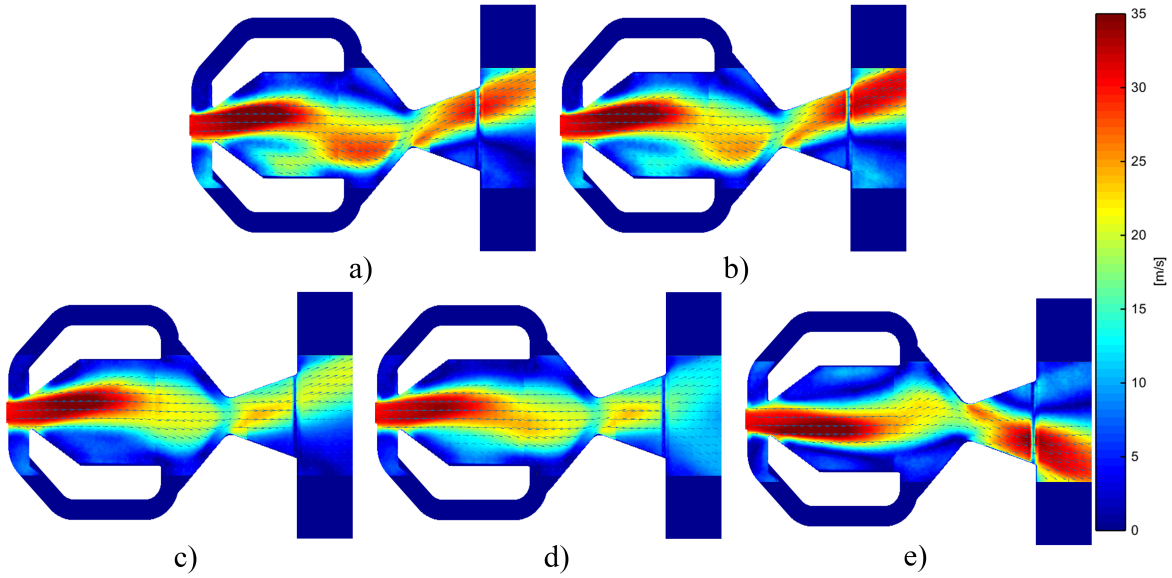

Figure 3.15: Experimentally determined velocity contours for the double feedback oscillator at a phase of a) 0, b) $\pi/4$, c) $\pi/2$, d) $3\pi/4$ and e) π

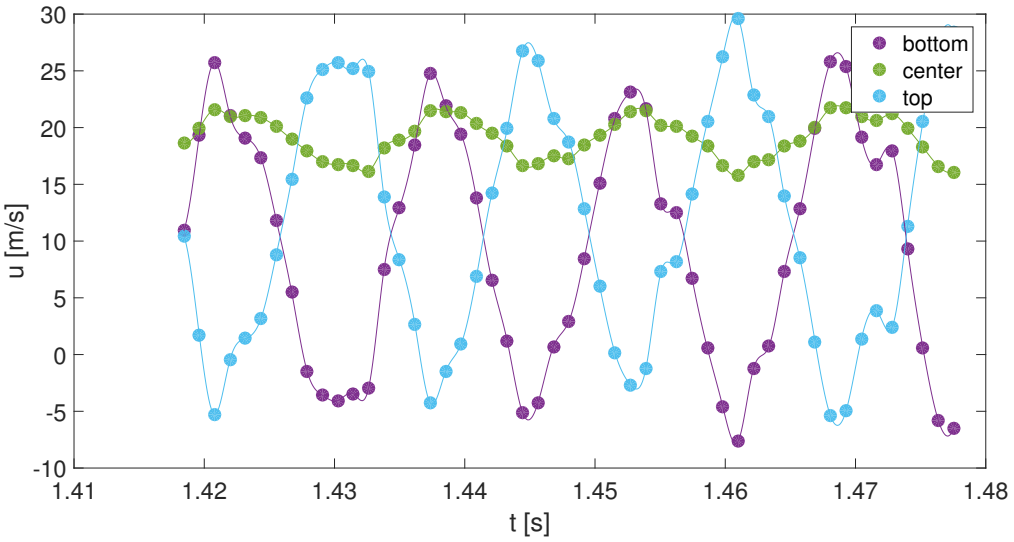

Figure 3.16: Experimentally determined velocities in x-direction at the exit centre, 4.26 mm above the exit center and 4.26 mm below the exit center of the DFO

Figure 3.16 shows the velocities in x-direction for three different vertical positions at the exit (see figure 2.8 for the positions). When the jet is fully deflected at the exit, peak velocities around 25 m/s are being reached near the walls. The velocity at the exit center position slightly sways around 20 m/s in phase with the main oscillation, but does not show the same amount of variation as the exit centre velocity of the numerical results in figure 3.11. The DFO only shortly touches upon the outer extreme deflections and immediately begins to travel to the opposite direction afterwards. When a maximum velocity is reached at one side of the exit the other is always negative, indicating a strong recirculation within the exit nozzle at the opposite side of the jet. During every oscillation cycle there are bumps in the exit velocity profile, most clearly visible after the last peak of the bottom probe velocity in figure 3.16. As these deviations from a clean oscillation appear approximately three times per oscillation they could be causing the second peak in the frequency amplitude spectrum of figure 3.14.

3.2.3 Oscillation frequencies

Although the internal flow is only shown for a single flow rate in the previous sections, the DFO was measured and simulated at several inlet flow rates. The range spanned by the experiment is significantly smaller than what has been simulated, as the simulations do not share the same practical limitations such as the maximum pressure that can be handled by the settling chamber and cyclone seeder. Similar to the results for the SFO, the frequency dependency upon the inlet flow rate shown in figure 3.17 is a linear relation for both the experimental and numerical results. In this case the measured frequencies of the experiments are higher than the simulated frequencies, having an average deviation of 42%. The gradient of the frequency

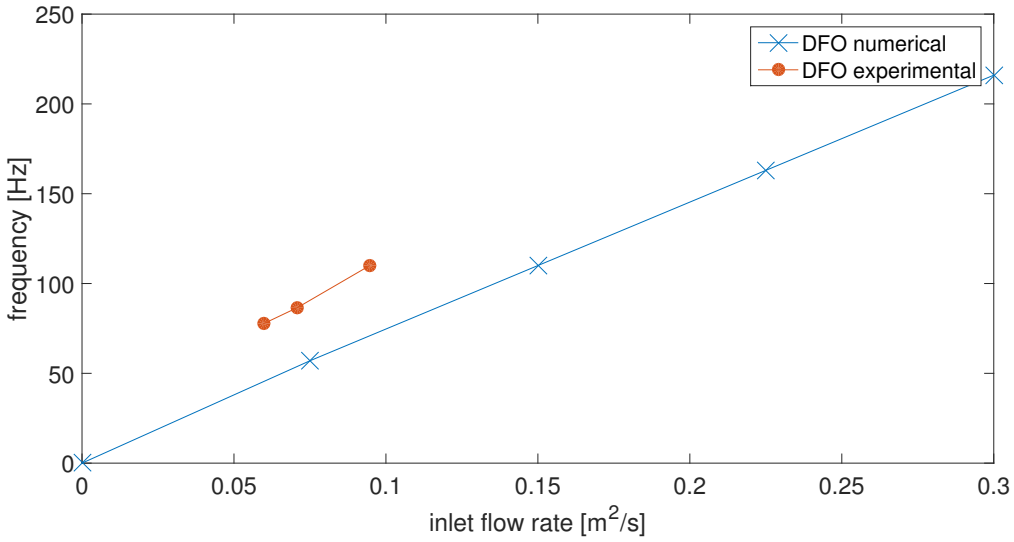

Figure 3.17: Frequency dependence upon inlet flow rate for the double feedback oscillator

dependence upon inlet flow rate of the experimental results for the DFO does correspond to the numerical results. Furthermore, it can be noted that the experimental curve would not pass through zero if extended to lower inlet flow rates, thus indicating a constant error in the inlet flow rates extracted from the measurement. The indicated frequencies at the exit do not depend upon the measured velocity magnitude and are thus more accurately determined, which is reflected by the high and narrow peak in the frequency amplitude spectrum.

3.3 Feedback free oscillator (FFO)

The numerical and experimental results for the feedback free oscillator are presented here, showing velocity contours and exit velocities in x-direction for both methods. The oscillation frequencies as a function of inlet flow rates are presented in the last part of this section, providing a means to quantitatively compare the experimental and numerical results.

3.3.1 Numerical results

The internal velocity contours for half an oscillation cycle of the feedback free oscillator simulated at an inlet flow rate of 0.150 m^2/s are shown in figure 3.18. The exit jet oscillates at a frequency of 507 Hz, which is more than twice as high as the SFO and almost five times as high as the DFO for the same inlet flow rate. Although the oscillating frequency is high, the time step size of $1 \cdot 10^{-6}$ s corresponds to roughly 2 000 time steps per oscillation. The internal flow field of the FFO does not appear to be symmetrical during an oscillation cycle, as opposed to the SFO and DFO where the internal flow field at $\phi = \pi$ is the mirror image

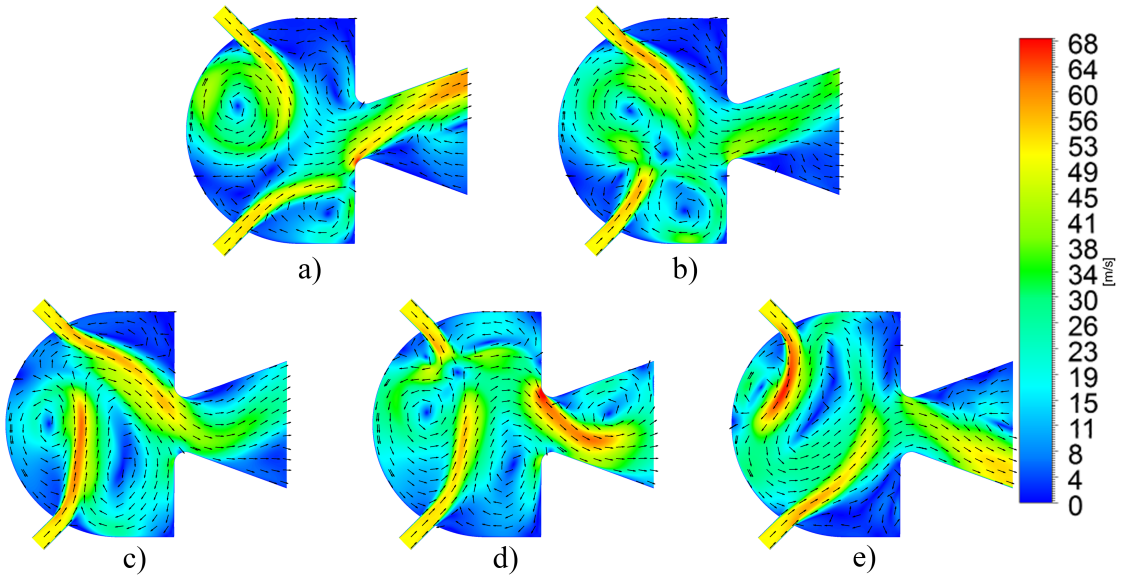

Figure 3.18: Numerically determined velocity contours for the feedback free oscillator at a phase of a) 0, b) $\pi/4$, c) $\pi/2$, d) $3\pi/4$ and e) π

of the flow field at $\phi = 0$. This could be an initiation effect of the oscillation in the numerical simulations, where a fully symmetric oscillation would be obtained after more time steps. For this reason the simulations of the FFO presented here were extended to 45 000 time steps, whereas the simulations of the SFO and DFO only required 6 000 time steps to capture a symmetric oscillation. Nevertheless the asymmetry is still present, with the calculation of even more time steps being too time consuming.

Despite the asymmetry in the internal flow, the velocity profiles at the exit depicted in figure 3.19 do show a stable oscillation. The peak velocities at both extreme deflections are relatively high compared to the velocity of the jet when passing through the exit center, with the asymmetry of the internal flow being reflected by a difference in exit velocity magnitude between the top and bottom probe position. The jet does not seem to remain attached to the diverging exit nozzle walls for long and immediately starts moving back to the other side when reaching an extreme deflection. The exit jet thus has a very short stay phase and a relatively long detachment phase. The attachment phase overlaps with the detachment phase, as flow already adheres to the divergent wall near the exit throat while the remainder of the pulse is still leaving the exit at the opposite side (see figure 3.18 *c*) . Because of the low center velocity and fast switching the flow at the exit more closely resembles two pulsed jets than a sweeping jet.

3.3.2 Experimental results

The relative energy entrained in the POD modes for the FFO at an inlet flow rate of 0.058 m^2/s shown in figure 3.20 is largest for the first mode and rapidly declines for successive

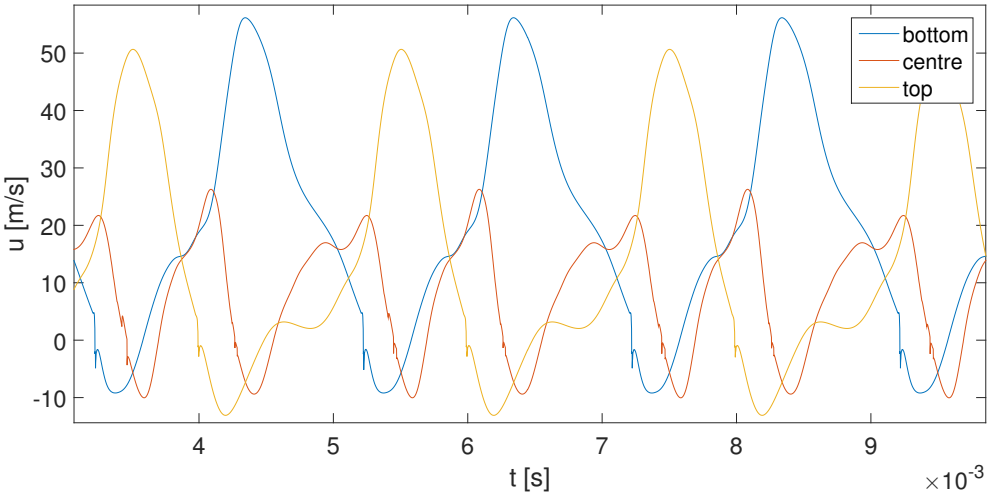

Figure 3.19: Numerically determined velocities in x-direction at the exit centre, 4.26 mm above the exit center and 4.26 mm below the exit center of the FFO

modes. The first two modes that are used to reconstruct the flow fields contain 49% of the total energy. The cumulative energy (figure 3.20) approaches an asymptotic value as expected, leaving only very little energy in the 1950 modes not shown in the figure.

The mean velocity contour of figure 3.21 (a) shows the exit nozzle being fully utilized as opposed to the SFO, although the largest amount of air exits through the centre. Being a larger frame, the internal area in which the inlet jets move is also clearly visible. A negative mean velocity in both corners of the mixing chamber indicates persistent circulation in these regions. The dark blue regions in the mixing chamber for both RMS velocity contours in figure 3.21 are shadows created by the build-up of seeding material inside the mixing chamber. The highest velocities in the RMS velocity contour (figure 3.21 c) are being reached through the exit centre, indicating only little time spend by the jet in fully deflected position.

The internal flow of the feedback free oscillator was captured using two different fields of view in separate measurements. The mean two-dimensional inlet flow rate was 0.058 m^2/s, with an oscillation frequency at the exit of approximately 258 Hz as it is the peak of the amplitude spectrum shown in figure 3.22. The lower temporal resolution has resulted in a scattered frequency amplitude spectrum, which has been filtered using Welch's method for clarity. The enlarged field of view required to capture this fluidic oscillator resulted in a dropped sampling rate of 846 Hz. Combined with the relatively high oscillation frequency of 258 Hz this essentially means that less than three images were taken during every oscillation cycle. As the oscillation frequency is still below the Nyquist rate and the sampling frequency was not phase-locked to the oscillation frequency, a full oscillation cycle could be reconstructed from all 2000 images over the duration of a measurement. The selected images of the different phases shown in figure 3.23 are thus in fact taken several hundreds of seconds apart in different oscillation cycles, showing the best correspondence to the phase of oscillation on a fitted

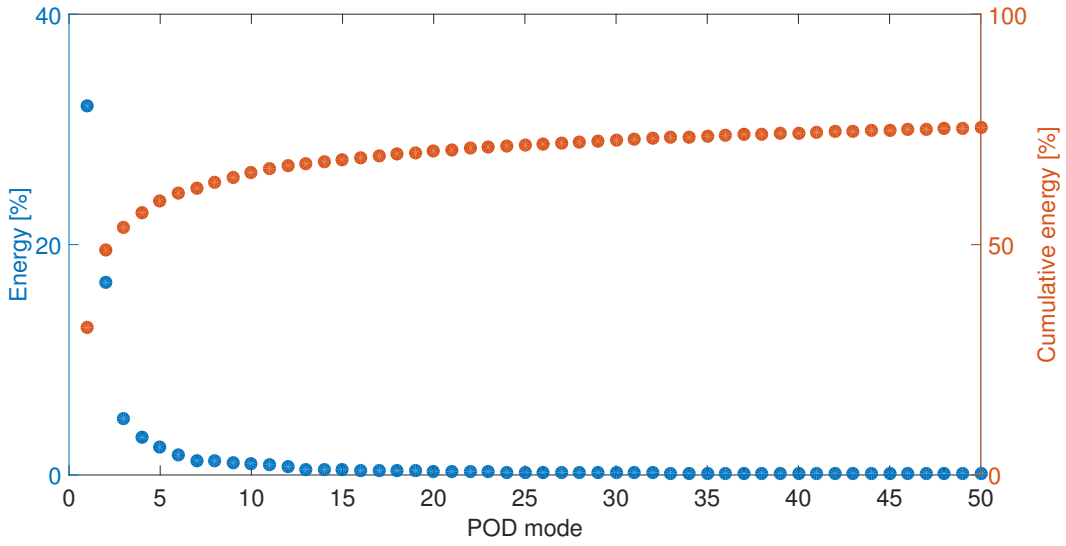

Figure 3.20: Relative and cumulative energy of the first 50 POD modes for the FFO at an inlet flow rate of 0.058 m^2/s

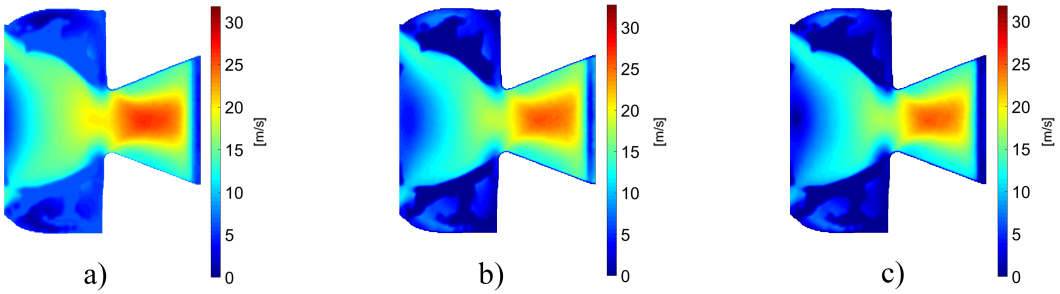

Figure 3.21: Close-up of the experimental results at the exit for the FFO with a) mean velocity contour from POD, b) RMS velocity contour from PSV vector fields and c) RMS velocity contour from POD

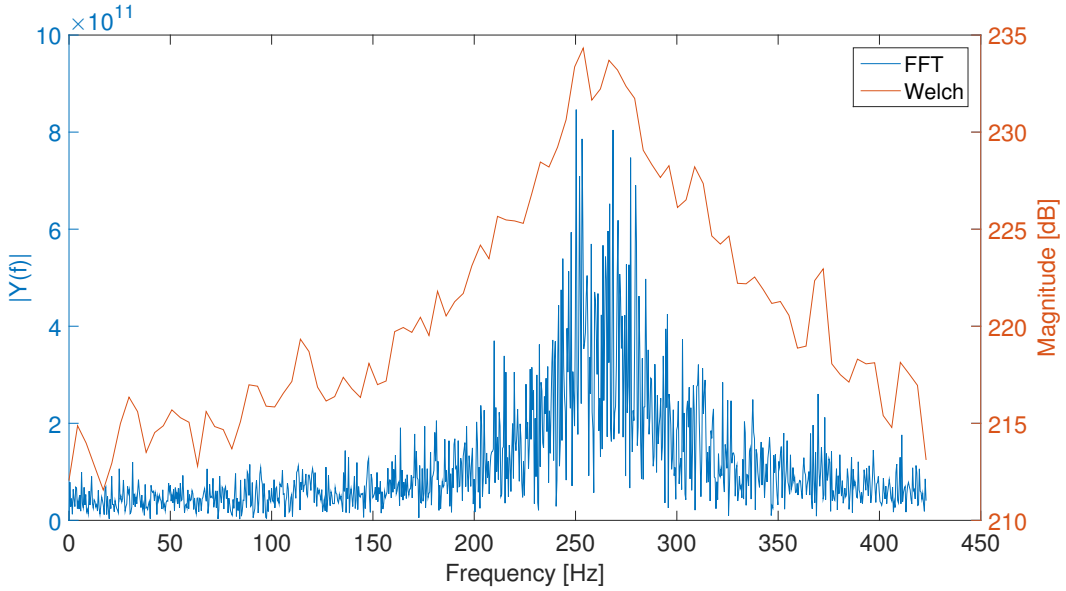

Figure 3.22: Frequency amplitude spectrum for the FFO at an inlet flow rate of 0.058 m^2/s and oscillation frequency of 258 Hz.

sine function. During the experiments it was noted that it took several seconds for the FFO to reach a stable oscillation, as opposed to the SFO and DFO that started oscillating immediately after opening the pressure valve. A similar behaviour was found during the numerical simulations.

While the exit jet in figure 3.23 (a) is still in the top position, the jet inside the mixing chamber coming from the top inlet has already deflected the jet originating from the bottom inlet towards the bottom of the oscillator. As time progresses, the bottom jet regains strength and starts pushing the top jet towards the top of the oscillator. Just when the bottom jet becomes dominant in the mixing chamber, the exit jet has switched to the bottom side as well. Inside the mixing chamber a large recirculation is always present in the left part near the curved wall, although switching direction during the oscillation cycle. This differs slightly from the flow field in this area shown by Tomac and Gregory (2013) measured in water, which could be due to the differences in geometry. Unfortunately, build-up of seeding material on the walls of the oscillator prevented accurate measurements of the flow in the top and bottom corners of the oscillator and inside the inlet channels.

The low temporal resolution of the measurement means that the variation of x-velocities with time fitted through the scarce measurement data would not provide meaningful information on the exit flow characteristics. Therefore, the velocities in the three probe positions for the FFO are reconstructed using the entire measurement set. This is done by slicing the entire measurement in pieces of approximately seven oscillation cycles and determining the dominating frequency in each slice by means of a fast Fourier transform. Slices that do not exactly correspond to the main oscillation frequency are disregarded, leaving 40 slices with seven oscillation cycles to reconstruct the data in this case. These data sets are then

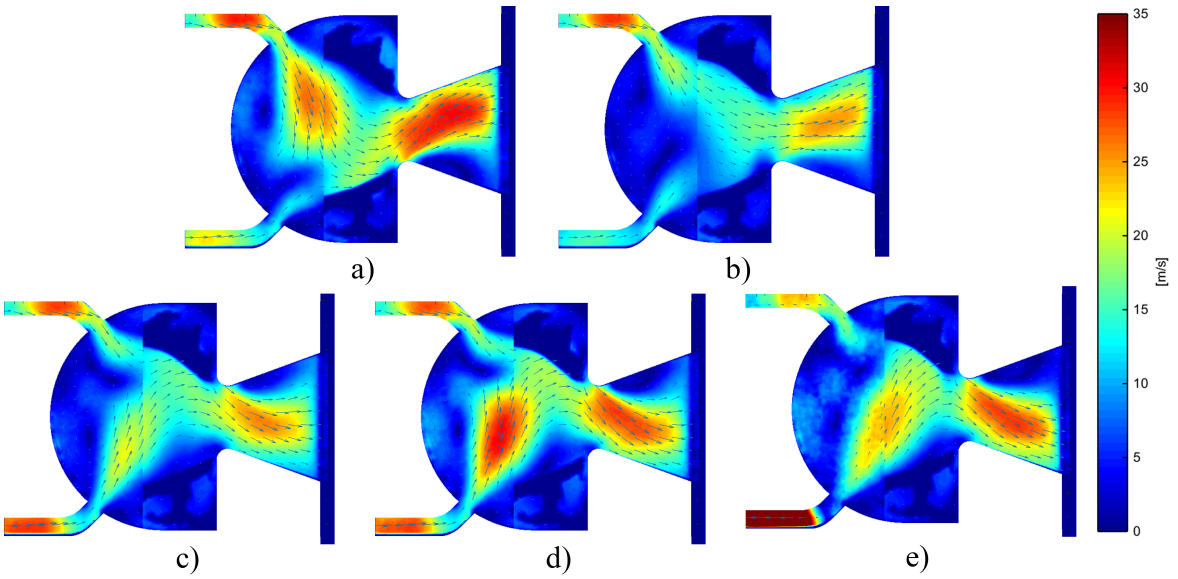

Figure 3.23: Experimentally determined velocity contours for the feedback free oscillator at a phase angle of a) 0, b) $\pi/4$, c) $\pi/2$, d) $3\pi/4$ and e) π

overlapped using the oscillation frequency. The resulting exit velocities at the probe positions as fitted through the data are shown in figure 3.24, including a shaded RMS error over the shown range.

Although the data shown in figure 3.24 is not conclusive, it does correspond with the numerical results shown in figure 3.19 in having a very short stay phase. These short pulses of high exit velocities at the most outward deflections are accompanied by a relatively constant flow through the exit centre that does not correspond with the numerical results. The detachment phase and attachment phase seem to be equal in duration, with negative velocities at the opposite sides of the attached flow indicating recirculation at the exit.

3.3.3 Oscillation frequencies

The feedback free oscillator could only be measured at a single inlet flow rate due to the high oscillating frequency at the exit, but a range of flow rates was simulated numerically. The dependence of the oscillation frequency at the exit upon this inlet flow rate is shown in figure 3.25. Again there is a linear relation as with the SFO and DFO, albeit at a much steeper slope. The single experimental measurement does not agree with the simulated curve, deviating from the interpolated numerical result at the same inlet flow rate by 43.2%. Combined with the large deviations seen for the SFO and DFO this means that the error in measured inlet flow rate for the FFO PSV experiments is also expected to be relatively large.

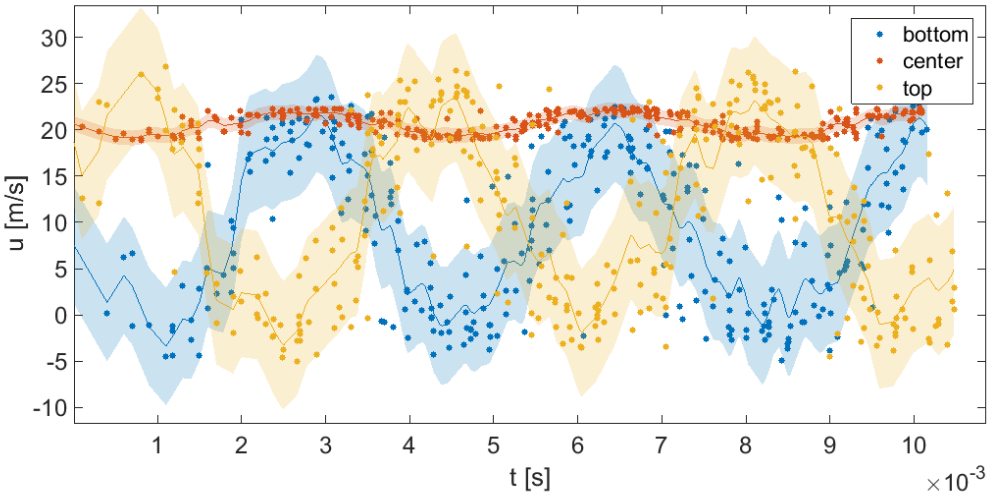

Figure 3.24: Experimentally determined velocities in x-direction reconstructed from the entire measurement range with shaded RMS error, 4.26 mm above the exit center and 4.26 mm below the exit center of the FFO

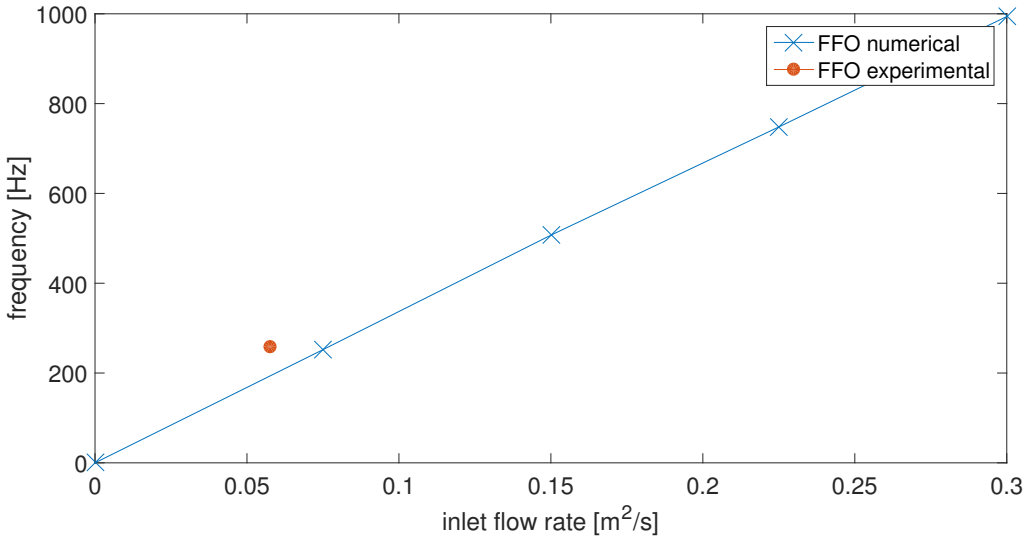

Figure 3.25: Frequency dependence upon inlet flow rate for the feedback free oscillator

Chapter 4

Comparing oscillator types

Although the results from numerical simulations and experiments for all oscillators have already been discussed in previous chapters, a comparison of all these results was still missing. Using the numerical and experimental results, a qualitative comparison of the internal flow mechanics will be discussed first, followed by a quantitative comparison of the flow rates and resulting oscillating frequencies. From this relatively large parameter range an empirical model is derived, relating the oscillator internal surface area and inlet flow rate to an oscillation frequency. This model is introduced in the last section of this chapter.

4.1 Internal flow mechanics

Although the internal flow mechanics differ greatly between the fluidic oscillator types discussed here, warranting their distinction, there are characteristics that can be compared when relating them to the resulting flow at the exit nozzle. The internal flow mechanics greatly influence the jet deflection and oscillating behaviour at the exit, but also the amount of energy required to operate the fluidic oscillators. Although the required energy was not measured during the experiments, the internal flow fields shown in the previous chapter were all taken at approximately equal supply pressures. The resulting flow rates thus give an indication of the energy lost in the internal flow, although not quantifiable with reasonable accuracy.

With the inlet and exit of the SFO being directly connected by the feedback loop openings, there is little resistance within this oscillator. This also results in the highest flow rate compared to the other oscillators at an identical supply pressure. Where the DFO and FFO both have a jet from the inlet that is enclosed by a mixing chamber and another jet forming at the exit nozzle, the inlet jet of the SFO directly flows into the exit as illustrated in figure 3.6. This means that the inlet jet of the SFO has to be deflected enough over a very small distance to attach to either of the diverging exit walls. Although resulting in considerably more internal resistance, the internal movement of the jet inside the DFO and FFO allows for

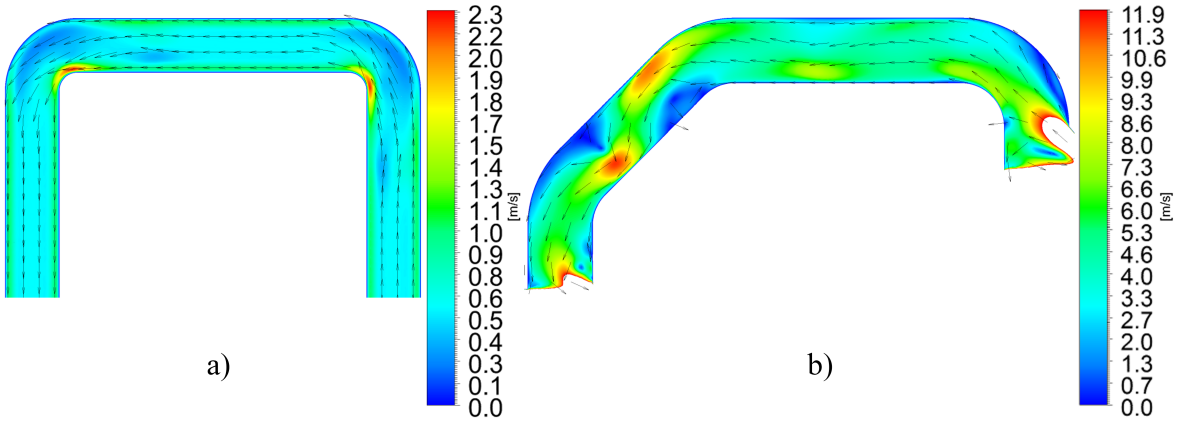

Figure 4.1: Flow inside the feedback tubes at $\phi = \pi$ of a) the SFO and b) the DFO from numerical simulations with an inlet flow rate of 0.150 m/s^2

greater jet deflections at the identical exit. Consequently, their oscillation is stronger with a lesser portion of the flow leaving through the exit centre as can be seen in the RMS velocity contours of the DFO in figure 3.13 (c) and the FFO in figure 3.21 (c). The flow rate of the FFO was lowest compared to the other types at an identical supply pressure. Having two inlets, the supply channel had to be split in front of the oscillator resulting in additional losses.

While the experimental results for both the DFO and FFO showed exit jets that were completely attached to one of the exit walls at full deflection (see figure 3.15 a and figure 3.23 a), the FFO only presents a relatively short pulse during an oscillation cycle compared to the longer stay of the DFO. This difference in behaviour can be explained by the two jets inside the FFO impinging on each other, with one jet essentially cutting the other in a small pulse before the process reverses. In figure 3.23 (a) and (e) the exit jet has just been 'cut'. The jet inside the mixing chamber of the DFO is never interrupted and is deflected towards an exit wall by the slanted surface leading to the exit nozzle as shown in figure 3.15 (a).

The influence of the feedback tubes differs greatly between the SFO and the DFO. As the experiments did not successfully capture the flow inside these tubes this can be best explained by comparing the numerically calculated internal flow fields shown in figure 4.1. A first observation is that the relative flow rate through the feedback loop is much higher for the DFO, with only very low flow velocities through the feedback loop of the SFO at full exit jet deflection. When looking at figure 3.1 the feedback loop of the SFO actually seems to suck air from the exit into the oscillator under the influence of the low pressure generated inside the feedback loop by the deflected jet. Although the flow rate inside the single feedback loop is low, it does suffice to detach the jet from the exit nozzle wall and move it in the opposite direction. The feedback loops of the DFO have a more complicated role in the internal flow mechanics of the oscillator, influencing the strength and position of the recirculation inside the mixing chamber to move the internal jet. The flow inside the feedback tube of the DFO as shown in figure 4.1 (b) is not very smooth, possibly influencing the flow patterns inside the main mixing chamber as well.

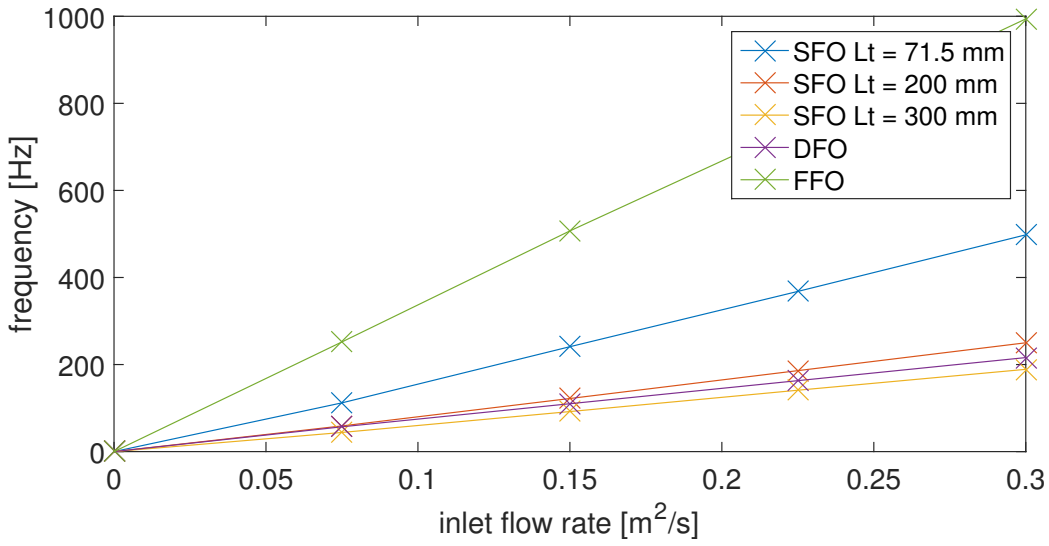

Figure 4.2: Comparison of oscillation frequencies versus flow rates as obtained by the numerical simulations

4.2 Flow rates and frequency

The relation between inlet flow rates and resulting oscillating frequencies for all three oscillator types as obtained from the numerical simulations is shown in figure 4.2. There is a very clear linear relation between the two quantities, although the slope varies between the oscillator types. The FFO reaches significantly higher oscillating frequencies for identical inlet flow rates, even when the internal surface area is higher than that of the SFO with a feedback tube length of 71.5 mm. The frequency of the SFO can be tuned very easily for a given inlet flow rate by changing the length of the feedback tube. Changing the width of the feedback tube possibly has a similar effect, although not verified in the current investigation.

The DFO shows similar oscillation frequencies to the SFO when their internal surface areas are within the same range, although the characteristics of the jet at the exit are very different. The SFO exit jet tends to steadily remain at one extreme deflection for a large part of half an oscillation cycle, while the exit jet of the DFO shows an unsteady extreme deflection with a relatively long portion of half an oscillation cycle being spend switching from one side to the other. The exit jet of the FFO also spends most time in between extreme deflections, showing large velocity peaks when an extreme deflection is reached.

The numerically simulated frequencies of the fluidic oscillators are compared to the experimental results obtained at different inlet flow rates in figure 4.3. The results for the SFO are only shown for a tube length of 200 mm as the influence of varying the feedback tube length was already shown in figure 4.1. The slope of the frequency response for varying inlet flow rates agrees very well between the experiments and numerical simulations, while the relatively large error in measured inlet flow rates is a possible explanation for the constant deviation

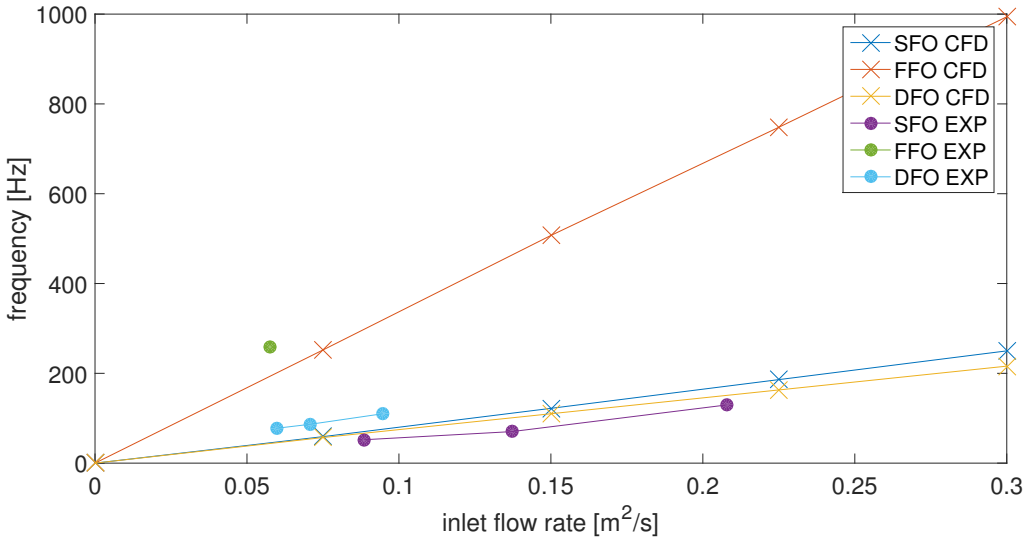

Figure 4.3: Oscillating frequencies versus two-dimensional flow rates for both experimental and numerical results of the three different oscillators. The results for the SFO with a feedback tube length of 200 mm are shown.

from the numerical results.

4.3 Empirical modelling

Using the resulting oscillating frequencies for the parameters spanned by the numerical simulations presented here an empirical relation can be formulated to obtain the oscillation frequency of a two-dimensional oscillator using air as the working fluid. The empirical relation is based on the formulation of the Strouhal number, using an area (A) and two-dimensional flow rate (q) instead of a characteristic length and velocity in the original equation. This differs from the previously proposed Strouhal number independence of bi-stable fluidic oscillators as can be found in the work of Tesa and Peszynski (2013) for example, which is based on the main inlet width and bulk velocity. This alternative approach can be formulated as

$$S = \frac{fA}{nq}, \tag{4.1}$$

with n being the number of inlets on the oscillator, q the two-dimensional flow rate in m^2/s and A the total surface area in m^2. The calculated values of S for all simulated oscillators are shown in table 4.1.

The values for S in the table are very close given the range of geometrical and flow rate variables, meriting the introduction of an empirical value. Therefore equation 4.1 is rewritten

oscillator type	L [mm]	A [mm^2]	q [m^2/s]	f [Hz]	S
SFO	71.5	318.7	0.075	112	0.476
SFO	71.5	318.7	0.150	241	0.512
SFO	71.5	318.7	0.225	368	0.521
SFO	71.5	318.7	0.300	498	0.529
SFO	200	704.2	0.075	59	0.554
SFO	200	704.2	0.150	122	0.573
SFO	200	704.2	0.225	186	0.582
SFO	200	704.2	0.300	251	0.589
SFO	300	1004.2	0.075	44	0.589
SFO	300	1004.2	0.150	92	0.616
SFO	300	1004.2	0.225	141	0.629
SFO	300	1004.2	0.300	189	0.633
DFO	71.5	633.6	0.075	57	0.482
DFO	71.5	633.6	0.150	110	0.465
DFO	71.5	633.6	0.225	163	0.459
DFO	71.5	633.6	0.300	216	0.456
FFO	-	343.0	0.075	252	0.576
FFO	-	343.0	0.150	507	0.580
FFO	-	343.0	0.225	748	0.570
FFO	-	343.0	0.300	994	0.568

Table 4.1: Calculated values of S for the numerical results of all oscillators

to obtain an oscillation frequency

$$f = \frac{nqS}{A}, \tag{4.2}$$

with S the empirically derived number with a value of 0.554. The value of S was chosen such that the average error in oscillation frequency when modelling the fluidic oscillators presented here is lowest. The predicted frequencies are compared to the frequencies obtained by the numerical simulations in figure 4.4, showing reasonable accuracy. The average deviation from the simulated result is 9.76%, with the best being 0.01% and the worst 17.65%. It has to be noted that the oscillator geometries presented here were designed to be comparable and the empirical value has not been validated for variations to the oscillator geometries presented here or different families of oscillators. Nevertheless, the relation shows a strong interaction between oscillator surface area, inlet flow rate and oscillating frequency that will be useful to predict the basic properties of a fluidic oscillator.

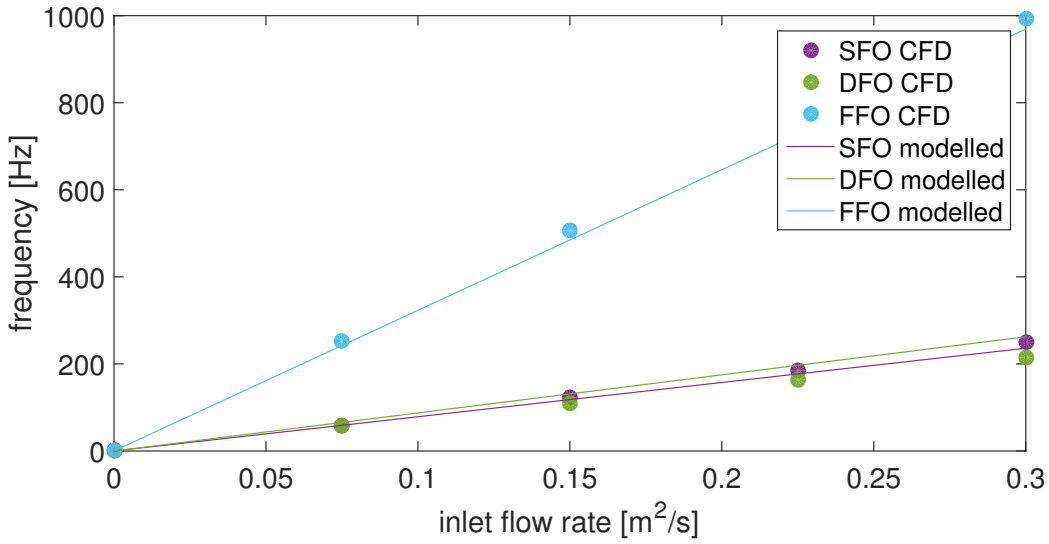

Figure 4.4: Empirically modelled fluidic oscillator frequencies using $S = 0.544$, compared to numerical simulation results.

Chapter 5

Conclusions

The PSV technique proved to be very effective in capturing the internal flow patterns of different fluidic oscillator types. Using cornstarch particles as the seeding material in combination with a high powered LED light source produced images with sufficient contrast. Although the flow following properties of these particles do not match more traditional seeding particles such as oil smoke, they are sufficient for the relatively low flow rates and corresponding oscillating frequencies discussed here. As seeding density was not very consistent over time and a large amount of measurement noise was introduced by contamination of the translucent walls and reflections it was essential to clean the transient data with the proper orthogonal decomposition technique. Using only the two highest modes from the proper orthogonal decomposition to reconstruct the velocity vectors provided clean images with clearly visible flow patterns. To visualize the entire internal flow field of the DFO and FFO multiple frames were captured during separate measurements and stitched together by looking for a best match in the overlapping region within all reconstructed velocity contours from the measurements.

Due to its simple internal geometry the SFO showed significantly higher flow rates than the other two oscillator types at comparable inlet pressures. A drawback of this simple switching mechanism is the inability to deflect the jet to large angles. The DFO and FFO perform significantly better in this aspect, having no difficulty to deflect the exit jet to the full exit nozzle divergence angle of 20°. The DFO additionally shows a steady transition from one extreme deflection to the other, where the SFO tends to stick to one side for some time and then switch relatively fast. Having a smooth transition is beneficial when a large area behind the jet should be influenced by the oscillating flow, while fast transition resembles two pulsating jets at an angle to each other. If the equivalent of two pulsating jets is desired at high operational efficiencies the SFO geometry can be optimized as shown by Arwatz et al. (2008a), having a smaller exit divergence angle with a splitter plate preventing airflow through the centre.

Although both the SFO and DFO are bi-stable fluidic oscillators and have feedback loops, their internal working mechanisms differ greatly. When deflected, the jet of the SFO is bend

at the location of the feedback loop, with air moving faster on the inside of the bend. The faster moving air results in a lower pressure at that side of the feedback tube, sucking air from the feedback tube into the main jet. The air from the feedback loop that is entrained in the main jet at full deflection can only be replenished by a positive flow into the feedback loop on the other side, thus creating a cross-flow that pushes the jet in the opposite direction. The numerical results of the DFO showed much higher velocities inside the two feedback loops compared to the SFO at identical inlet flow rates, greatly influencing the recirculation patterns inside the mixing chamber. As the velocities inside the feedback loop are higher, one can conclude that its shape will have a larger influence on the behaviour of the DFO. The relatively sharp corners in the feedback loop of the DFO presented here result in separated flow regions inside the loop as shown in the numerical results, possibly effecting the oscillator's performance. The internal flow mechanics of the FFO were best visualized by the numerical simulations, as the PSV experiments showed poor temporal resolution. Nevertheless, both the numerical simulations and experimental measurements on the FFO show the internal jets being cut into small pulses at the exit, with recirculation patterns inside the mixing chamber moving the internal jets back and forth.

Numerical simulations proved to be a very efficient way of comparing the characteristics of the three different oscillators for a relatively large parameter range, although the simulated frequency versus flow rate curves deviate from the experimental results with approximately 40% for all oscillators. The two-dimensional numerical simulations did show similar internal flow characteristics to the experimental visualisation. It is clear that the oscillating frequencies increase linearly with increasing flow rates, showing no signs of reaching a limiting value within the inspected range. A large range of oscillation frequencies can be reached for subsonic inlet velocities by the fluidic oscillators presented here. The FFO reaches the highest oscillation frequency for a given inlet flow rate, while the frequency of the SFO can be tuned by altering the feedback tube length.

Based on the internal surface area, inlet flow rate and oscillation frequency an empirical model was derived representing the family of two-dimensional oscillators presented here. The calculated frequencies using the empirical model showed good agreement with the simulated oscillators over the entire inlet flow rate range, with an average error in modelled frequency of less than 10%. This raises confidence in extending the empirical model to variations of the fluidic oscillator geometries presented here, although the influence of matched inlet and exit nozzle dimensions might not be negligible.

Chapter 6

Recommendations

Although interesting and valuable results have been obtained during the current investigation into the internal flow of fluidic oscillators, there are some aspects that can be improved upon in future research. In general, the fluidic oscillators have proven to be very robust and adaptable during the experiments presented in this text, certainly warranting further investigations into their operating scope and application.

6.1 Numerical simulations

- The constant uniform velocity profile provided at the inlet should be replaced by a profile matching the boundary layers as measured during the experiments that is allowed to fluctuate in magnitude.
- Geometrical variations to the family of oscillators presented here should be simulated to provide a more complete scope of operating ranges and to validate the empirical model for a larger range.
- The asymmetrical internal flow of the FFO on a fully symmetric mesh is probably not physical and its origins should be investigated.
- A wider range of flow rates can be investigated

6.2 Experimental investigation

- The experiments fully relied on the data that can be extracted from the PSV measurements. Adding pressure taps at different locations and measuring the mass flow rate into the oscillators would reduce the margin of error in the presented data significantly.

- The FFO was not measured at a sufficiently high temporal resolution to obtain accurate results. Measurements at a significantly higher sampling rate would resolve this issue.
- Higher luminous intensity from the LED would increase the contrast between particle shadows and contaminants, reducing measurement noise. The LED was not operated at full power during the measurements, giving a possibility to further improve measurement noise.
- The amount of seeding from the cyclone seeding device was not steady and difficult to control. An improvement of the seeding device would result in less acquisition runs that need to be redone.
- Using a fixed value of two modes to reconstruct the flow field from the POD for all oscillators results in different amounts of relative energy of the captured field being used for reconstruction. The amount of modes used should be based on the amount of energy entrained, especially since the oscillation frequency might not be constant during a measurement.
- Although the 450 L wooden box used as a small settling chamber worked very well, it did slightly expand under pressure. It could be improved by further bracing or a complete redesign.

6.3 Application for active flow control

Although the application of the fluidic oscillators was not investigated, some of the properties presented here do translate to recommendations that could be useful when looking into the application of these devices.

- As shown, the oscillators have the ability to operate at a wide range of frequencies. Oscillating frequencies always translate to sound and thus noise, which might not be acceptable for all applications. During the measurements, the lower operating frequencies seemed to be produce less noise. This could be interesting to investigate.
- The exit velocity profiles largely differ between the different types of oscillators. The different oscillator types are thus possibly suitable for different applications. Both the operation as two pulsating jets or as a sweeping jet should be effective in controlling boundary layer separation, although efficiency may vary. This can be investigated experimentally by implementing a variety of fluidic oscillator geometries on an identical aerodynamic shape.

Bibliography

G. Arwatz, I. Fono, and A. Seifert. Suction and oscillatory blowing Actuator Modeling and Validation. *AIAA Journal*, 46(5), 2008a. doi: 10.2514/1.30468.

G. Arwatz, I. Fono, and A. Seifert. Suction and oscillatory blowing actuator. *Solid Mechanics and its Applications*, 7:33–44, 2008b. ISSN 18753507. doi: 10.1007/978-1-4020-6858-4{_}4.

B. C. Bobusch, R. Woszidlo, J. M. Bergada, C. N. Nayeri, and C. O. Paschereit. Experimental study of the internal flow structures inside a fluidic oscillator. *Experiments in Fluids*, 54 (6), 2013a. ISSN 07234864. doi: 10.1007/s00348-013-1559-6.

B. C. Bobusch, R. Woszildo, O. Kruger, and C. O. Paschereit. Numerical Investigations on Geometric Parameters Affecting the Oscillation Properties of a Fluidic Oscillator. *AiAA 2013-2709*, pages 1–15, 2013b. doi: 10.2514/6.2013-2709.

L. M. M. Boermans. Research on sailplane aerodynamics at Delft University of Technology . Recent and present developments . *Technical Soaring*, 30(1-2):1–25, 2006.

F. T. Brown. A Combined Analytical and Experimental Approach to the Development of Fluid-Jet Amplifiers. *Journal of Basic Engineering*, 86(2):175, 1964. ISSN 00219223. doi: 10.1115/1.3653023.

N. A. Buchmann, C. Willert, and J. Soria. Tomographic Particle Image Velocimetry using Pulsed, High Power LED Volume Illumination. In *17th Australian Fluid Mechanics Conference*, number December, 2010.

L. N. Cattafesta and M. Sheplak. Actuators for Active Flow Control. *Annual Review of Fluid Mechanics*, 43(1):247–272, 2011. ISSN 0066-4189. doi: 10.1146/annurev-fluid-122109-160634.

J. Estevadeordal and L. Goss. PIV with LED: Particle Shadow Velocimetry (PSV). *43rd AIAA Aerospace Sciences Meeting and Exhibit*, ill:1–10, 2005. doi: 10.2514/6.2005-37.

D. Feikema and D. Culley. Computational Fluid Dynamic Modeling of a Fluidic Actuator for Flow Control. *46th Aerospace Sciences Meeting and Exhibit*, (January):AIAA 2008–557, 2008.

M. Gad-el Hak. Flow Control. *Applied Mechanics Reviews*, 42(10):262–293, 2013.

S. Gärtlein, R. Woszidlo, F. Ostermann, C. N. Nayeri, and C. O. Paschereit. The Time-Resolved Internal and External Flow Field Properties of a Fluidic Oscillator. *AIAA SciTech 52nd Aerospace Sciences Meeting*, (January):1–15, 2014. doi: 10.2514/6.2014-1143.

P. H. Geoghegan, N. A. Buchmann, J. Soria, and M. Jermy. High-speed LED-illuminated PIV measurements of the time-dependent flow field in a stenosed, compliant arterial model. *16th International Symposium on Applications of Laser Techniques to Fluid Mechanics*, 2012.

S. A. Gokoglu, M. A. Kuczmarski, D. E. Culley, and S. Raghu. Numerical Studies of a Supersonic Fluidic Diverter Actuator for Flow Control. *NASA 5th Flow Control Conference*, (July):1–16, 2010a. doi: doi:10.2514/6.2010-4415.

S. A. Gokoglu, M. A. Kuczmarski, D. E. Culley, and S. Raghu. Numerical Studies of a Fluidic Diverter Actuator for Flow Control. *Aiaa 2010-4415*, (July):1–16, 2010b. doi: doi:10.2514/6.2010-4415.

D. Greenblatt and I. J. Wygnanski. Control of flow separation by periodic excitation. *Progress in Aerospace Sciences*, 36(7):487–545, 2000. ISSN 03760421. doi: 10.1016/S0376-0421(00)00008-7.

J. Kim and P. Moin. Detailed simulation of turbulent flow within a suction and oscillatory blowing fluidic actuator. *Center for Turbulence Research, Annual Research Briefs*, pages 209–217, 2014.

M. Koklu and L. P. Melton. Sweeping Jet Actuator in a Quiescent Environment. *AIAA Abstract*, pages 1–21, 2012. doi: 10.2514/6.2013-2477.

R. Mei. Velocity fidelity of flow tracer particles. *Experiments in Fluids*, 22(1):1–13, 1996. ISSN 0723-4864. doi: 10.1007/BF01893300.

F. Ostermann, R. Woszildo, S. Gärtlein, C. N. Nayeri, and C. O. Paschereit. Phase-Averaging Methods for a Naturally Oscillating Flow Field. *Aiaa 2014-1142*, (January), 2014. doi: 10.2514/6.2014-1142.

S. Raghu. Feedback-free Fluidic Oscillator and Method, 2001.

R. Seele, P. Tewes, R. Woszidlo, M. A. McVeigh, N. J. Lucas, and I. J. Wygnanski. Discrete Sweeping Jets as Tools for Improving the Performance of the V-22. *Journal of Aircraft*, 46(6):2098–2106, 2009. ISSN 0021-8669. doi: 10.2514/1.43663.

R. Seele, E. Graff, M. Gharib, L. Taubert, J. C. Lin, and I. Wygnanski. Improving Rudder Effectiveness with Sweeping Jet Actuators. *6th AIAA Flow Control Conference*, (June):1–12, 2012. doi: 10.2514/6.2012-3244.

A. Seifert, T. Bachar, D. Koss, M. Shepshelovich, and I. Wygnanski. Oscillatory Blowing: A Tool to Delay Boundary-Layer Separation. *AIAA Journal*, 31(11):2052–2060, 1993. ISSN 0001-1452. doi: 10.2514/3.49121.

A. Seifert, O. Stalnov, D. Sperber, G. Arwatz, V. Palei, S. David, I. Dayan, and I. Fono. Large Trucks Drag Reduction Using Active Flow Control. *46th AIAA Aerospace Sciences Meeting and Exhibit*, 2008. doi: 10.2514/6.2008-743.

T. Shtendel and A. Seifert. Three-dimensional aspects of cylinder drag reduction by suction and oscillatory blowing. *International Journal of Heat and Fluid Flow*, 45(1):109–127, 2014. ISSN 0142727X. doi: 10.1016/j.ijheatfluidflow.2013.10.009.

V. Tesa and K. Peszynski. Strangely behaving fluidic oscillator. *APJ Web of Conferences*, 45(01074), 2013. ISSN 2100-014X. doi: 10.1051/epjconf/20134501074.

M. N. Tomac and J. W. Gregory. Jet Interactions in a Feedback-Free Fluidic Oscillator in Low Flow Rate Region. *AIAA 43rd Fluid Dynamics Conference*, pages 1–10, 2013. doi: 10.2514/6.2013-2478.

H. Viets. Flip-Flop Jet Nozzle. *AIAA Journal*, 13(10):1375–1379, 1975.

E. Wagner, R. Furlan, M. Tadeu, L. de Sistemas, and I. Escola. Numerical Analysis of a Microfluidic Oscillator Flowmeter Operating with Gases or Liquids. *Technical Proceedings of the Fifth International Conference on Modeling and Simulation of Microsystems*, (3): 2–5, 2002.

R. E. Wagner. Fluidics-a new control tool. *IEEE Spectrum*, 6(11), 1969. ISSN 0018-9235. doi: 10.1109/MSPEC.1969.5214171.

F. Wassermann, D. Hecker, B. Jung, M. Markl, A. Seifert, and S. Grundmann. Phase-locked 3D3C-MRV measurements in a bi-stable fluidic oscillator. *Experiments in Fluids*, 54(3): 1–10, 2013. ISSN 07234864. doi: 10.1007/s00348-013-1487-5.

C. Willert, S. Moessner, and J. Klinner. Pulsed Operation of High Power Light Emitting Diodes for Flow Velocimetry. *8th International Symposium On Partcle Image Velocimetry - PIV09*, pages 5–8, 2009.

C. Willert, B. Stasicki, J. Klinner, and S. Moessner. Pulsed operation of high-power light emitting diodes for imaging flow velocimetry. *Measurement Science and Technology*, 21(7): 075402, 2010. ISSN 0957-0233. doi: 10.1088/0957-0233/21/7/075402.

J. Wilson, D. Schatzman, E. Arad, A. Seifert, and T. Shtendel. Suction and Pulsed-Blowing Flow Control Applied to an Axisymmetric Body. *AIAA Journal*, 51(10):2432–2446, 2013. ISSN 0001-1452. doi: 10.2514/1.J052333.

Appendix A

Designing the final geometries

The design iterations as performed to arrive at the final fluidic oscillator geometries are discussed in this appendix, trying to justify the final geometries as they were used for the numerical simulations and experimental measurements. The single feedback loop oscillator is discussed first, followed by the design process for the double feedback oscillator and feedback free oscillator.

The single feedback oscillator was the first two-dimensional geometry that was created during the current investigation, largely based on the single feedback oscillator used by Arwatz et al. (2008a) in combination with an ejector to form the suction and oscillatory blowing oscillator. This first geometry had a relatively long exit nozzle with a splitter plate and a divergence angle of 12°. There was a large chamber behind the oscillator in order to capture the exit flow, which proved to increase the computational time significantly. As the focus is on the internal flow of the fluidic oscillators the chamber was omitted for all following geometries. Making the feedback loop shorter and wider provided a more realistic dimension considering the tubes that could be used as feedback loops in experiments, resulting in a new version of single feedback oscillator.

The last considerable change in the geometry was focussed on the exit nozzle, omitting the splitter plate and giving it a larger divergence angle of 20°with a 6 mm nozzle throat width. This was mainly done because the splitter influenced the exit flow field, making it less obvious what the contribution of the internal flow mechanics is. The larger divergence angle gives larger deviations of the exit jet position, making it easier to track its movement. The geometry of the throat was later rounded and varied in width between 2 mm and 6 mm. All oscillators performed well in the numerical simulations with an exit throat width of 4 mm, which was therefore chosen as the common exit geometry for the simulations and experiments. The feedback loop length was matched to the total length of the feedback loops of the DFO and later varied to include simulations with a feedback loop length of 200 mm and 300 mm as measured during the experiments.

Taking the design as presented by Gärtlein et al. (2014) as the starting point and working on the same scale as the first designs of the single feedback oscillator meant less design iterations were needed to arrive at the final double feedback oscillator geometry. The feedback loop corners were rounded as suggested by Bobusch et al. (2013b) and the exit nozzle dimensions were taken to match the SFO.

It took a bit more effort to arrive at a suitable geometry for the feedback free oscillator, especially since it was very hard to find a geometry that oscillates at all. It turns out that it takes a lot longer for the FFO to initialize a sustained oscillation compared to the SFO and DFO, which might also explain earlier designs being disregarded as not working properly. During this process, especially the exit nozzle was changed a lot. Varying from a slit to a straight exit nozzle with multiple opening dimensions to finally arrive at the shared diverging exit nozzle for all oscillators. As the oscillation depends on the interaction of the two jets inside the mixing chamber, care was taken to ensure a structured and refined mesh in this region to keep the Courant number low.

Appendix B

Overview of numerical simulations

h [mm]	L [mm]	q [m^2/s]	timesteps	dt [s]	f [Hz]
4	71.5	0.075	6000	$5 \cdot 10^{-6}$	112
4	71.5	0.150	6000	$5 \cdot 10^{-6}$	241
4	71.5	0.225	6000	$5 \cdot 10^{-6}$	368
4	71.5	0.300	6000	$5 \cdot 10^{-6}$	498
2	71.5	0.075	6000	$5 \cdot 10^{-6}$	does not oscillate
2	71.5	0.150	6000	$5 \cdot 10^{-6}$	does not oscillate
2	71.5	0.225	6000	$5 \cdot 10^{-6}$	does not oscillate
2	71.5	0.300	6000	$5 \cdot 10^{-6}$	does not oscillate
4	200	0.075	8865	$5 \cdot 10^{-6}$	59
4	200	0.150	6000	$5 \cdot 10^{-6}$	122
4	200	0.225	6000	$5 \cdot 10^{-6}$	186
4	200	0.300	6000	$5 \cdot 10^{-6}$	254
4	300	0.075	10000	$5 \cdot 10^{-6}$	44
4	300	0.150	9690	$5 \cdot 10^{-6}$	92
4	300	0.225	6000	$5 \cdot 10^{-6}$	141
4	300	0.300	6000	$5 \cdot 10^{-6}$	189

Table B.1: Simulation results for the SFO with h the exit throat width, L the feedback tube length, q the inlet flow rate and f the oscillation frequency.

h [mm]	L [mm]	q [m^2/s]	timesteps	dt [s]	f [Hz]
2	71.5	0.075	6000	$5 \cdot 10^{-6}$	65
2	71.5	0.150	6000	$5 \cdot 10^{-6}$	117
2	71.5	0.225	6000	$5 \cdot 10^{-6}$	171
2	71.5	0.300	6000	$5 \cdot 10^{-6}$	226
4	71.5	0.075	6000	$5 \cdot 10^{-6}$	57
4	71.5	0.150	6000	$5 \cdot 10^{-6}$	110
4	71.5	0.225	6000	$5 \cdot 10^{-6}$	163
4	71.5	0.300	6000	$5 \cdot 10^{-6}$	216

Table B.2: Simulation results for the DFO with h the exit throat width, L the feedback tube length, q the inlet flow rate and f the oscillation frequency.

h [mm]	q [m^2/s]	timesteps	dt [s]	f [Hz]
2	0.075	6000	$5 \cdot 10^{-6}$	246
2	0.150	6000	$5 \cdot 10^{-6}$	448
2	0.225	6000	$5 \cdot 10^{-6}$	631
2	0.300	6000	$5 \cdot 10^{-6}$	846
4	0.075	50000	$1 \cdot 10^{-6}$	252
4	0.150	30000	$1 \cdot 10^{-6}$	507
4	0.225	25000	$1 \cdot 10^{-6}$	748
4	0.300	25000	$1 \cdot 10^{-6}$	994

Table B.3: Simulation results for the FFO with h the exit throat width, q the inlet flow rate and f the oscillation frequency.

Appendix C

Overview of PSV eperiments

Although each combination of fluidic oscillator geometry and captured frame was measured at least three times, the tables below only list the measurements that have been used to extract the data that has been presented in the previous chapters. Nevertheless, the corresponding file names are also included for future referencing of the data.

q [m^2/s]	f [Hz]	frame	L [mm]	Samp. Rate [Hz]	dt [μs]	file name
0.137	70	centre	200	1160	4	150811-133558
0.208	130	centre	200	1160	4	150811-161833
0.089	52	centre	200	1160	4	150811-172441
0.125	56	centre	300	1160	4	150811-181908
0.135	84	centre	150	1160	4	150812-133302

Table C.1: Overview of PSV experiments on the SFO

q [m^2/s]	f [Hz]	frame	L [mm]	Samp. Rate [Hz]	dt [μs]	file name
0.071	97	inlet	71.5	1160	4	150803-173749
0.071	97	centre	71.5	1160	4	150803-182311
0.071	97	exit	71.5	1160	4	150803-190043
0.095	110	exit	71.5	1160	4	150805-105947
0.095	110	centre	71.5	1160	4	150805-113822
0.095	110	inlet	71.5	1160	4	150805-130542
40	78	inlet	71.5	1160	6	150806-112552
40	78	centre	71.5	1160	6	150806-115224
40	78	exit	71.5	1160	6	150806-123438

Table C.2: Overview of PSV experiments on the DFO

q [m^2/s]	f [Hz]	frame	L [mm]	Samp. Rate [Hz]	dt [μs]	file name
0.058	258	centre	-	846	4	150817-122334
0.058	258	inlet	-	846	4	150817-140243

Table C.3: Overview of PSV experiments on the FFO